This manuscript is a preprint.

.

This manuscript has been submitted to Coastal Engineering (ISSN 0378-3839).

Subsequent versions of this manuscript may have different content. If accepted, the final version of this manuscript will be available via the 'Peer-reviewed Publication DOI' link
via this webpage.

Please feel free to contact any of the authors directly or to comment on the manuscript. We welcome feedback!

Kees Nederhoff
Deltares USA
8601 Georgia Ave., Silver Spring, MD 20910, USA
Email: kees.nederhoff@deltares-usa.us

Tropical or extratropical cyclones: what drives the compound flood hazard, impact, and risk for the United States Southeast Atlantic coast?

Authors: Kees Nederhoff, Tim Leijnse, Kai Parker, Jennifer Thomas, Andy O'Neill, Maarten van Ormondt, Robert McCall, Li Erikson, Patrick L. Barnard, Amy Foxgrover, Wouter Klessens, Norberto C. Nadal-Caraballo, Chris Massey

Outlet: Coastal Engineering

Abstract

Subtropical coastlines are impacted by both tropical and extratropical cyclones. While both may lead to substantial damage to coastal communities, it is difficult to determine the contribution of tropical cyclones in coastal flooding relative to that of extratropical cyclones. We conduct a large-scale flood hazard and impact assessment across the subtropical Southeast Atlantic Coast of the United States, from Virginia to Florida, including different flood hazards. The physics-based hydrodynamic modeling skillfully reproduces coastal water levels based on a comprehensive validation of tides, almost two hundred historical storms, and an in-depth hindcast of Hurricane Florence. We show that yearly flood impacts are two times as likely to be driven by extratropical than tropical cyclones. On the other hand, tropical cyclones are thirty times more likely to affect people during rarer 100-year events than extratropical cyclones and contribute to more than half of the regional flood risk. With increasing sea levels, more area will be flooded, regardless if that flooding is driven by tropical or extratropical cyclones. Most of the absolute flood risk is contained in the greater Miami metropolitan area. However, several less populous counties have the highest relative risks. The results of this study provide critical information for understanding the source and frequency of compound flooding across the Southeast Atlantic Coast of the United States.

Introduction

A large and growing share of the world's population lives in coastal regions and is vulnerable to extreme events, such as tropical cyclones. Merkens et al. (2016) estimated that 680 million people live in the low-lying coastal zone worldwide and that this amount could reach more than one billion by 2050. The high concentration of people in coastal areas has resulted in many economic benefits, including improved transportation, industrial and urban development, revenue from tourism, food production, and many more. However, this also concentrates vulnerability to natural hazards in the coastal zone. Moreover, humans are not the only species in the coastal regions that can be affected by extreme events. Beaches, dunes, and tidal wetlands are diverse ecosystems in the coastal zone that are sensitive to climate change and extreme events. For example, Dewald and Pike (2014) showed that hurricanes affect 97% of the sea turtle nesting beaches in the Northwestern Atlantic and Northeastern Pacific Oceans.

Sea-level rise (SLR) increases coastal flooding (e.g., Vitousek et al., 2017; Taherkhani et al., 2020; Sweet et al., 2022). Coastal flooding is driven by many complex factors. In addition to changes in sea level, flooding can occur because of storms, high tides (king tides[1]), or a combination of the two. Storms, both tropical cyclones (TCs) and extratropical cyclones (ETCs), can result in storm surge, high waves, and rainfall that can contribute to or result in flooding. Moreover, the intensity, duration, and occurrence of these storm impacts are expected to change in the coming decades due to climate change. For example, as a consequence of a warmer waters and a warmer more humid atmosphere, Knutson et al. (2015) showed that global average TC intensity, rainfall rates, and occurrence of very intense TCs are projected to increase. In addition, global climate models show a projected poleward

[1] King tide is a popular colloquial term to describe exceptionally high tides that occur during a new or full moon

shift in midlatitude ETC tracks, with varying changes in the strength of storms across the globe (Chang et al., 2012; Chemke et al., 2022).

In recent years, more focus has been given to compound flooding, caused by the co-occurrence of high tides, coastal storm surges, waves, precipitation, and/or river discharge (Wahl et al., 2015). Storm events, such as Hurricane Florence (2018), have highlighted the importance of compound events and the need to include all relevant drivers of flooding to assess local and regional coastal flood risk. Hurricane Florence resulted in large amounts of rainfall in North and South Carolina. For example, locally, Swansboro and Elizabethtown, N.C., recorded close to 90 cm, or more than 30 inches (Callaghan, 2020). Rainfall together with other drivers resulted in a large compound flood zone in the low-lying coastal zone where ocean, precipitation, and river discharge were all of importance (Ye et al., 2021). However, a priori, the relative contribution of each physical driver to the flooding is often unknown. Whereas flooding hazards from each physical process may be realized, quantifying hazards due to the combination of two or more processes is difficult due to a large number of possible combinations and non-linear physical interactions (e.g., Huang et al., 2021). One solution is to apply multivariate extreme value theory, which requires dynamic downscaling of many events to define the critical region where flooding occurs. Ideally, all possible combinations need to be simulated by either the use of extensive computational resources or computationally efficient methods. Computationally efficient methods can be achieved by an acceleration of the direct simulations, developing a series of event reduction techniques, or by a combination of the two, for example, through hybrid downscaling (Bakker et al., 2022).

In addition to the general challenges of modeling compound flooding (Santiago-Collazo, et al., 2019), estimating return periods (RPs) of TC-included flooding remains a significant obstacle. This challenge is related to two factors. First, TCs are poorly resolved in many synoptic-scale and global climate datasets used for meteorological forcing due to coarse spatial and temporal resolution, causing an underestimation in TC intensity (Roberts et al., 2020) and, consequently, storm surge and wave conditions (Murakami and Sugi, 2010). Second, the limited record length of available meteorological forcing data, in combination with the low probability of TCs, means the number of TCs is too small to estimate RPs robustly (e.g., Lin and Emanuel, 2016; Leijnse et al., 2022). In flood risk assessment, it is possible to overcome some of these limitations via synthetic emulation of TC tracks (e.g., Vickery et al., 2000; Bloemendaal et al., 2020; Nederhoff et al., 2021) or other statistical techniques such as the joint probability method (JPM; Resio and Irish, 2015). Still these approaches suffer from parameterizations of key physics (e.g., land-sea interactions or sea water temperature) and are based on datasets with limited temporal length. Alternatives could be the pseudo-global warming approach (Jyoteeshkumar Reddy et al., 2021) or the full dynamical approach (Mori et al., 2016), this last only available to a few nationwide research centers with very high computing capacity (Mori et al., 2021).

In recent years, the scientific community has increasingly focused on (TC-induced) compound events. In all these efforts, coupling procedures between marine (tide and surge) and inland processes (rainfall and riverine discharge) are paramount to capture the complex physical interactions. For example, at the local-watershed scale, Gori et al. (2020) simulated all the physical iterations of multiple flood drivers for many synthetic TC events to produce probabilistic hazard maps, including a breakdown of rainfall versus surge-dominated flood zones. Bates et al. (2021) took this one step further and provided the first integrated and high-resolution view of U.S. fluvial, coastal, and pluvial flood hazard, as a single layer, driven by both TC and ETC events. However, that study did not provide an estimate of the contribution of TCs to compound flooding. Booth et al. (2016) provided a breakdown between TCs and ETCs for the U.S. mid-Atlantic and Northeast Coasts based on observational data and showed that TCs typically dominate the most extreme events (e.g., 100-year event) while more common events (e.g., yearly) driven by ETCs are equally important. To

the knowledge of the authors, no study has yet estimated the relative contribution of TCs and ETCs to compound flooding using an integrated physics-based model that encapsulates inland and coastal processes across thousands of kilometers.

In this paper, we introduce, validate, and apply a workflow for analyzing and predicting compound flooding hazards, impacts, and risks for both tropical and extratropical cyclones. This approach is applied on large spatial scales and for dozens of realizations in the future climate and for seven SLR scenarios. This work is part of a broader project led by the U.S. Geological Survey to map future coastal flooding and erosion hazards across the Southeast United States due to SLR and storms in a changing climate. This work focuses on the overland coastal flooding component of the study. The novelty of this manuscript is investigating the contribution of TC and ETC events to flood hazards and how this will change with SLR. The paper is structured as follows. First, we describe the regional domain in this study. Second, the materials and methods applied in this workflow are described. Third, the results are presented, which a) focus on the validation of tide, historical conditions, and Hurricane Florence, and b) on the application of the model to assess flood hazards and impacts on the future climate and SLR scenarios. Lastly, we present our discussion and conclusions sections.

The Southeast Atlantic coastal zone

The Southeast Atlantic Coast includes vast stretches of coastal and inland low-lying areas, the southern reach of the Appalachian Mountains, several high-growth metropolitan areas (e.g., Miami, Jacksonville, Savannah, Charleston, Wilmington, and Norfolk), and large rural expanses. This study focuses on the coastal zone of the Southeast Atlantic Coast, ranging from the Florida Keys in the south up to the mouth of the Chesapeake Bay in the north (gray counties shown in Figure 1A). The coastal zone is manually defined here as the area between the current shoreline and about the 10 m elevation contour relative to NAVD88. This Low Elevation Coastal Zone (McGranahan et al., 2007) typically extends about 100 km inland in this region.

The Southeast Atlantic Coast is rapidly urbanizing. For example, Southeast Atlantic Coast contains many of the fastest-growing metropolitan areas in the country, including several of the top 20 fastest-growing urban regions in 2020 (U.S. Census, 2020). This shift is on top of existing sizeable urban city centers such as the greater Miami area (Miami-Dade, Broward, and Palm Beach counties). These trends toward a more urbanized Southeast are expected to persist, creating new vulnerabilities by increasing population exposure to areas in the flood hazard zone (e.g., 100-year flood map).

Flood hazards are expected to increase in the future due to rising global sea levels (Vitousek et al., 2017, Taherkani et al., 2020; Sweet et al., 2022). The average global mean sea level (GMSL) has risen about 21-24 cm from 1880 to 2021 and are 97 mm above 1993 levels (NOAA, 2022). Moreover, its rise has been accelerating since 1990 (Dangendorf et al., 2017, Sweet et al., 2022). Moreover, GMSL rise is projected to continue to accelerate due, for example, to the increased mass loss of the Antarctic ice sheet (Le Bars et al., 2017). Recent downscaled projections for Southeast Atlantic Coast by Sweet et al. (2022) suggested rates and an increase in local sea levels, relative to the 2000 range, of 0.3-0.5 m for 2050, 0.5-1.6 m for 2100, and 0.7-2.7 m for 2150. This will significantly alter flooding frequency in many already vulnerable communities.

Many cities across the Southeast Atlantic Coast are starting to plan for the impacts rising waters are likely to have on their infrastructure. For example, flood events in Charleston, S.C., have been increasing and are projected to increase substantially more in the future with sea-level rise; the city has prepared a Sea-Level Rise Strategy Plan (City of Charleston, 2015). The city is also planning to undertake subsequential steps to further protect the city and its inhabitants from nuisance flooding.

Besides high tide events, which will be augmented due to SLR, the Southeast Atlantic Coast is regularly impacted by extreme weather events. TCs can bring strong winds, heavy rainfall, and high surge and waves in the summer and fall. Some of these TCs, such as Hurricane Andrew (1992), were extremely powerful and have devastated communities in the Southeast Atlantic Coast. ETC events can also trigger a large amount of flooding due to wind and precipitation and subsequent storm surge and high waves. For example, during the October 2015 event, a significant rainfall nor'easter caused historic flash flooding across North and South Carolina, resulting in $2.5 billion in damages (NCEI, 2022). Hurricane Florence in 2018 resulted in $24 billion in wind and water damage (NHC, 2022).

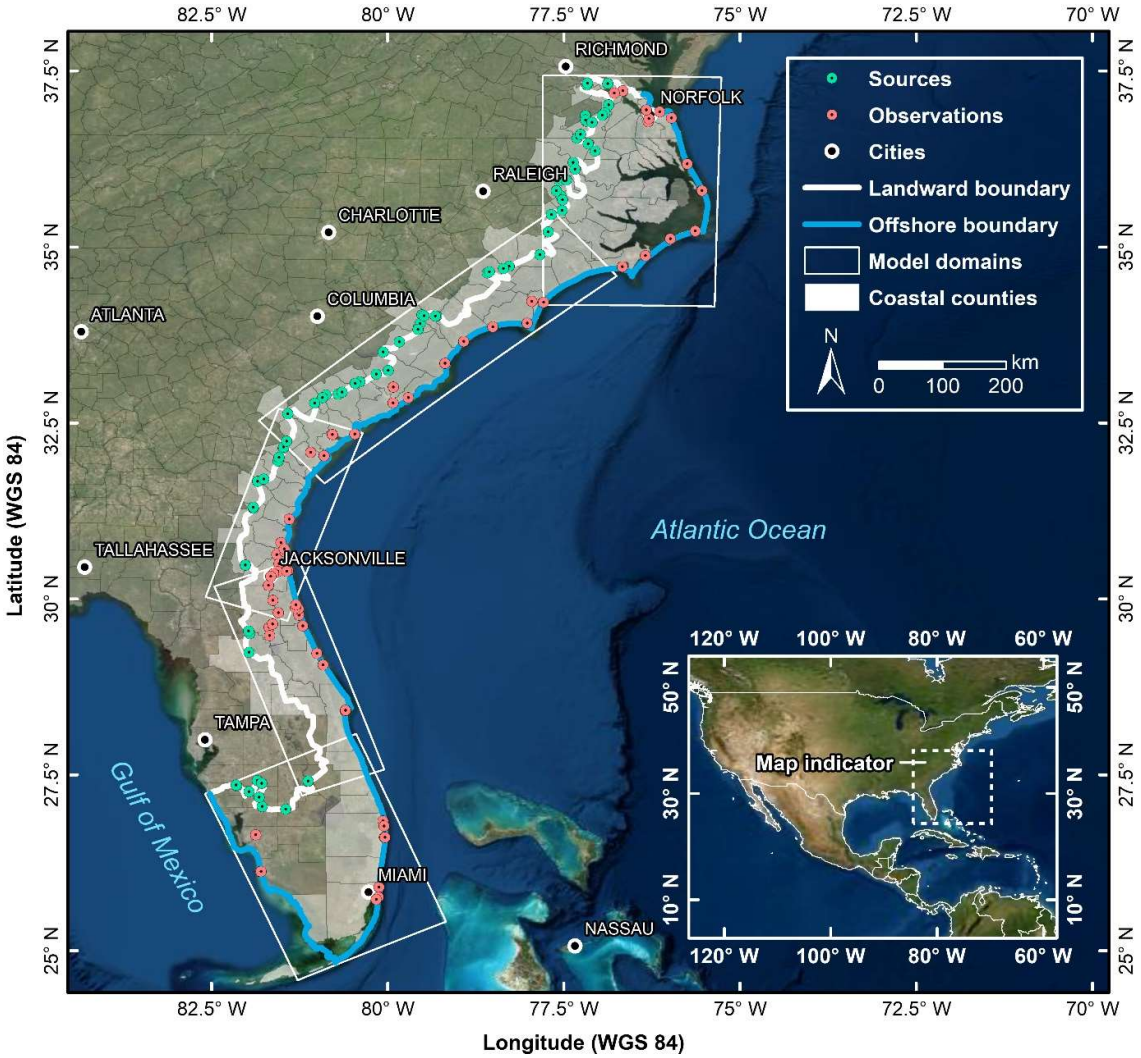

Figure 1. The study area (shown in gray) consists of the coastal counties in the United States Southeast Atlantic Coast states of Florida, Georgia, South Carolina, North Carolina, and parts of Virginia. Also, shown are the SFINCS (Super-Fast Inundation of CoastS) flood model domains (white outlines), offshore boundary (blue line), sources (green dots), and observation points (red dots). Model domains typically reach about 100 km inland to about 10 m above NAVD88 (the landward boundary of the model in white). Several major city names are presented to orient the reader. © Esri, DigitalGlobe, GeoEye, i-cubed, USDA FSA, USGS, AEX, Getmapping, Aerogrid, IGN, IGP, swisstopo, and the GIS User Community.

Materials and methods

Overview

The modeling approach is based broadly on the Coastal Storm Modeling System (CoSMoS: Barnard et al., 2014; 2019, Erikson et al., 2018; O'Neill et al., 2018), initially developed for the West Coast of the United States, but with significant modifications and updates to address the need to capture and resolve TCs as well as pluvial contributions to flooding. The numerical computation of overland flooding is based on the open-source overland flood model SFINCS (Super-Fast INundation of CoastS; Leijnse et al., 2021) and includes infiltration processes. We created five computational domains for the study region (Figure 1). The SFINCS domains were run for tens of thousands of emulated storms. This approach was followed for two reasons: First, to determine model skill and, in particular, accuracy for validation purposes (Section 'Results-Validation') and secondly, to assess spatial compound flood hazards on a cell-by-cell basis for future climate conditions (Section 'Results – Flood hazards and impact'). The latter includes a breakdown of the contribution of TC versus ETCs. Required input data and individual methodological and model components are described below, followed by detailed explanations of the numerical methods and computational framework.

Input data

Topo-bathymetry, soil type, land cover

Before generating the overland flood models, elevation datasets were extracted along the entirety of the Southeast Atlantic Coast from the area's Coastal National Elevation Database (CoNED) topographic model (Danielson et al., 2016; Tyler et al., 2022), Continuously Updated Digital Elevation Model (CUDEM; CIRES, 2014), and Coastal Relief Model (NOAA National Geophysical Data Center, 2001). Topo-bathymetric data were applied in the order listed to cover the entire area and fill data gaps. The model landward extent was manually determined to allow for minimal inflow boundary locations and typically reaches +10m elevation relative to NAVD88. The seaward extent was set to around NAVD88 – 10 m. This depth suffices for overland flood modeling purposes. Maximum dune elevations along the coast were derived from CoNED and cross-checked with Doran et al. (2021) to include as coastal flood defenses in the overland flooding models.

Information from the National Land Cover Database (Homer et al., 2020) was converted to roughness values using Manning's coefficients and approaches as described by Nederhoff et al. (2021) to define a spatially varying roughness map across each SFINCS model (see Table 2). Friction in open water was set to a typical coastal value of 0.020 and was thus not used for calibration purposes.

Data from U.S. General Soil Map (STATSGO2; U.S. Department of Agriculture; USDA, 2020) provided the input for the Curve Number infiltration method used in the overland flooding models. STATSGO2 is an inventory developed by the U.S. Department of Agriculture and includes soil characteristics information across the Continental U.S. The hydrologic soil group (HSG) information and hydraulic conductivity (Ks) from the surface layer were used for this study. In particular, HSG information was combined with a landcover map to estimate the curve numbers according to USDA (1986).

Boundary conditions: meteorological conditions, water levels, waves, discharges, and SLR

The atmospheric conditions for the historical (validation) period (1980–2018) were based on ERA5 (Hersbach et al., 2020) for wind and pressure in combination with the North American Land Data Assimilation System (NLDAS; Xia et al., 2012) for rainfall. For the projection period (2020–2050), conditions were applied from the Coupled Model Intercomparison Project - Phase 6 (CMIP6). In particular, an ensemble of three CMIP6 models was used from the High-Resolution Model Intercomparison Project (HighResMIP) based on the SSP5-8.5 greenhouse gas concentration scenario: CMCC-CM2-VHR4 (Scoccimarro et al., 2017), GFDL-CMC4C192 (Guo et al., 2018), and

HadGEM3 (Roberts, 2019). These models were chosen because of their increased atmospheric and ocean resolution of up to 25-50 km, which is expected to better resolve coastal storm events which cannot be adequately resolved with the native resolution of most GCMs (Roberts et al., 2020). The chosen CMIP6 models, at the time of this study, had data from 2020–2050. All 31 years of data of all three models were used for this study.

Multi-decadal-scale hindcast, reanalysis, and General Circulation Models, such as ERA5 and CMIP6-HighResMIP, allow for an analysis of the long-term evolution of the climate and how it affects global processes. However, model resolutions are often insufficient to fully resolve TCs and have a limited temporal length (see introduction). The U.S. Army Corps of Engineers (USACE) dataset (Nadal-Caraballo et al., 2020) for TCs was applied to overcome these limitations. Thousands of synthetic TCs were simulated. This method is based on Joint Probability Method (JPM) of the current climate. For more information on the JPM method, refer to Nadal-Caraballo et al. (2022). In the present study, the probabilities of the synthetic TCs were updated to reflect climate change in which more intense hurricanes are likely to be observed more frequently in the study area from northern Florida northward. This change is related to higher sea surface temperatures. For information on how this was done, one is referred to Thomas et al. (in preparation). Rainfall for TCs was based on the Interagency Performance Evaluation Task Force Rainfall Analysis (IPET, 2006) method. The IPET method relates pressure deficit to rainfall which decreases exponential as function of TC radii. Within the eye of the storm rainfall rates are constant. No asymmetry and/or rainfall band are included in this method.

For the historical periods, we assumed that ERA5-NLDAS had sufficient resolution to resolve TC activity for validation purposes (Dullaart et al., 2020). On the other hand, for the projection period, we assumed TC events were missing in CMIP6 and only ETCs were included (Han et al., 2022).

Water level time series were applied at the offshore boundary of the SFINCS models. Water level time series were derived from a linear superposition of statistically corrected Global Tide and Surge Model (GTSM; Muis et al., 2016, 2022) outputs and wave setup computed with a parameterized empirical formula (Stockdon et al., 2006) and waves from the ERA5 reanalysis (Hersbach et al., 2020) and projection time-periods (Erikson et al. 2022). Both the hydrodynamic and wave models were forced with the same CMIP6 models for the climate projections. For more information on the statistical-corrected GTSM and wave setup, refer to Parker et al. (in review). For the TC simulations, water levels from the coupled numerical hydrodynamic and wave model setup (ADCIRC+SWAN; see Nadal-Caraballo et al., 2022), which includes tide, wind-driven surge, and wave-driven setup, were used.

Discharges for 74 rivers flowing into the study domain were derived from the NOAA National Water Model (NWM) CONUS Retrospective Dataset (NOAA, 2021). This reanalyzed river discharge dataset was used directly for the historical (validation) period. River discharge for the projection period was derived using a relationship between NWM discharge and historical NLDAS precipitation and applying this relationship using CMIP6 projected precipitation to estimate future discharge rates. In particular, the upstream watershed location of each river was identified from the network of river-reach IDs used by the NWM (Liu et al., 2018). For each watershed, cumulative precipitation was computed and the best correlation using a linear fit with a variable time lag between cumulative daily precipitation and discharge was found. This linear fit was then applied to the precipitation from the CMIP6 models, yielding projected future discharge for each of the streams for each CMIP6 model. The projected future discharge was bias corrected, based on the historical NWM discharge using empirical quantile matching (Li et al., 2010). A baseflow, as calculated from NWM using a digital filter method from the HydRun toolbox (Tang and Carey, 2017), was also applied in the TC

simulations. Baseflow was included to get an estimate of discharge-driven compound flooding during TCs.

Exposure and vulnerability data

Impact computations for computed flood maps were performed with HydroMT-FIAT, an open-source python wrapper (Eilander & Boisgontier, 2022) for the Delft-FIAT flood impact and risk model. Delft-FIAT (Flood Impact Assessment Tool) is a flexible open-source toolset for building and running flood impact models which are based on the unit-loss method (De Bruijn, 2005). Inputs for FIAT are a hazard layer (water depth), exposure layer (object map with population), and vulnerability (depth-damage curves).

The exposure layer used in Delft-FIAT was based on a method that combines Global Urban Footprint (GUF; Esch et al., 2017) for the presence of buildings and the Global Human Settlement Layer (GHSL; Florczyk et al., 2019) for population density. In order words, the GHSL estimate the amount of people in certain areas, which are distributed over the building footprints provided by GUF. The result is a method that can produce an exposure layer for any place on the globe. In this paper, we calibrated the population per county using the 2020 Census, which resulted in a total population size of 18,828,520 for the area of interest. Vulnerability curves are based on Huizinga et al. (2020). Flood impact is defined here as the population affected via the vulnerability curve. Flood risk is defined as the product of the probability of a flood event and potential adverse consequences for humans (Kron, 2005).

Validation data

A comprehensive set of validation data was used to assess model skill. First, all observed 6-minute interval water levels from all long-term National Oceanic and Atmospheric Administration (NOAA) water level stations (CO-OPS, 2022) between 1980 and 2018 for the area of interest were collected and processed into continuous time series. In total, 24 NOAA stations were included in the validation (see Figure 1, Figure 2 or Figure 4 for their locations).

The observed water levels were used to determine tidal constituents using UTide (Codiga, 2011) for each NOAA gauge. In addition, the XTide database (retrieved via Delft Dashboard; van Ormondt et al., 2020) was also used to identify 68 locations with observed tidal amplitude and phases for model validation. See Figure 2 for the location of both the NOAA and XTide stations.

Special attention was given to validating Hurricane Florence (2018), which made landfall near Wilmington, N.C. For this singular event, an additional 156 pressure gauges and 396 high water marks (HWM) made available by the U.S. Geological Survey (USGS) were also used to validate the model (U.S. Geological Survey, 2021; see Figure 5 for their locations).

Numerical method: overland flooding with SFINCS

Overview

SFINCS (Leijnse et al., 2021) was successfully applied to simulate compound flooding, including dynamic hydraulic processes such as tidal propagation, rainfall, and river runoff while maintaining computational efficiency (e.g., Sebastian et al., 2021) and was therefore chosen to predict overland flooding for this study. The physics model dynamically computes water propagation throughout the domain with a computational time step of several seconds (varies per simulation). High-resolution topo-bathymetry and land roughness were included in the native 1x1 meter resolution utilizing subgrid lookup tables (Leijnse et al., 2020). The continuity and momentum computations were performed on a coarser 200x200 meter resolution grid to save computational expense. Subgrid bathymetry features were included to account for maximum dune height based on the DEM to control overflow during storm conditions. Leijnse et al. (2020) showed water level computations for

Hurricane Irma (2017) were still accurate when including subgrid features based on the high-resolution elevation data. The SFINCS model was not calibrated but instead applied with default parameters throughout this study. Advection was deactivated to save computational time but was not found to influence the results (typical in non-wave-driven flooding applications; Leijnse et al., 2021). Derived overland maximum flood levels were subsequently downscaled to 10x10 meter resolution water depths using the nearest neighbor interpolation for the water level in combination with a box filter of 3 neighboring grid cells. The five computational SFINCS domains overlap to overcome any possible boundary effects. Overlapping model domains were merged by taking the average water level. The water levels (described by the tide, non-tidal residual; NTR, and wave setup components) were imposed at the offshore boundary (see Figure 1 for the location). Incoming short and infragravity waves were not accounted for (except through statistical downscaling of wave setup from offshore wave conditions) since dynamical downscaling this was computationally prohibitive (increasing computation times ~1000-fold[2]). Implications of the model setup are described the in the discussion section.

Curve Number method

Infiltration was computed at every computational time step with the newly implemented Curve Number method in SFINCS. This method is based on the SCS (Soil Conservation Service, currently known as Natural Resource Conservation Service) Curve Number method for evaluating the volume of rainfall resulting in direct surface runoff. SCS was first developed in 1954 and is described in most hydrology handbooks and textbooks (e.g., Bedient et al., 2013). This method was added to SFINCS to take advantage of most practicing engineers' familiarity with this method and the availability of tabulated curve numbers for a wide range of land use and soil groups. The Curve Number method is a combined loss method that estimates the net loss due to interception, depression storage, and infiltration to predict the total rainfall excess from a rainfall event.

The Curve Number model uses the following equation to relate total event runoff *Q* to total event precipitation *P*.

$$\boldsymbol{Q} = \frac{(\boldsymbol{P} - \boldsymbol{I_a} \cdot \boldsymbol{S_{max}})^2}{\boldsymbol{P} + (\boldsymbol{1} - \boldsymbol{I_a})\boldsymbol{S_{max}}} \qquad \text{Equation 1}$$

$$S_{max} = \left(\frac{100}{CN} - 10\right) 0.0254 \qquad \text{Equation 2}$$

in which I_a is the initial abstraction percentage (default 20%), *CN* is the Curve Number, and *S* is the retention after runoff begins. Note that here we directly convert the original curve number in inches to meters via the computation of S_{max}. Since SFINCS is a continuous model, the Curve Number computation is done at a time-step level (order of seconds). It computes the infiltration rate by subtracting the total precipitation with runoff and dividing by the time step (forward differences).

The moisture storage capacity of the soil can be depleted during wet periods and replenished during dry periods. To model this behavior with the Curve Number method, whether it rains or not, we implemented the effective storage capacity (S_e), which is tracked during the simulation. During rainfall, the capacity is slowly filled (Equations 1 and 2). During a period with no precipitation, the effective moisture storage capacity is assumed to be replenished at a rate proportional to S_{max}. Here, we related the recovery constant to the soil saturation akin the approach used in the Storm Water Management Model (SWMM; U.S. Environmental Protection Agency, 2015). In particular, the

[2] The current model resolution is 200 meter. In order to resolve infragravity waves, a model resolution of at least 20 meters would be needed. This results in 100 times more grid cells compared to a 200-meter resolution. However, via the CFL condition this increases computational expense with a factor 100x10 = 1000x

continuous recovery k_r is estimated with the following equation $k_r = \sqrt{K_s}/75$, in which K_s is the hydraulic conductivity in inch/hr and k_r is the recovery in the percentage of S_{max} per hour. At the start of new simulations, the cumulative variables are reset to 0, and S_e is set equal to 50% of S_{max}.

Computational framework

Storm selection

Two slightly different approaches were followed to define the storms. The first one is used to define storms to be run in the validation period. The second one is used for the climate projection period.

First, using all the observed water level data between 1980 and 2018 retrieved from all NOAA tide gauges within the region, the observed linear sea level trend was removed from each individual gauge. Next, unique observed storm peaks were detected via the peak-over-threshold method by finding, on average, three maximum water levels yearly per gauge (39 years x 3 peaks = 117 peaks for most gauges). To guarantee independence between the storms, peaks at different gauges were considered a single storm if their lag in time is less than 7 days. This resulted in a total of 198 historical storms, used here for validation purposes. In regard to duration, each validation storm is run for at least seven days around the middle of the peak when the storm is characterized by a single peak, and for longer in case of containing multiple peaks. In this case, the minimum and maximum peak date define the duration of the storm and, consequently, the simulation time. In regard to the hydrograph characterization of the storm, the simulation starts at low water of NAVD88 – 0.5 m to avoid low-lying flooding areas since SFINCS initializes water levels across the domain based on the starting water level.

Second, for the 31 years of climate projection record, particular storms per CMIP6 model, were selected based on three independent criteria. In a similar fashion as for the observed data, for each offshore water level boundary point, we detect water level peaks in which the threshold is set to identify, on average, three maximum water level events yearly. A similar method to that one used for extreme sea level was used for discharge and rainfall. The peaks were identified for all 74 discharge points and for the total rainfall per SFINCS domain, combined, and run similarly to the validation runs. Common peaks were found as result of these methods; however, only the unique storms were combined per SFINCS domain, resulting in 263 to 347 events per domain per CMIP6 model. This method was chosen to reduce computational expense since, in this way, we simulated around ~20% of the total record and could run simulations in parallel. The main difference between both periods is that fluvial and pluvial data were included as criteria for selecting storms in the climate projection period. However, for the validation period the available validation data were limited to tide gauges and therefore, only these data were used to define storms.

For the TC runs, a total of 1059 tracks were included. Each track had a probability, location of landfall, heading, forward speed and intensity based on the synthetic dataset from Nadal-Caraballo et al. (2020). Specific TCs were neglected if a track resulted in less than 20 cm of storm surge everywhere in each domain. The number of neglected tracks varies per domain (799 to 933 from the total of 1059 were included).

Extreme value analysis

Flood hazards per numerical (SFINCS) grid cell was determined using empirical estimates of exceedance probabilities, without regressing return period estimates using any extreme value parametric distribution. In this way, the full set of potential candidates to compound flooding is simulated without making any a priori inference on the underlying processes beyond compound flooding (Anderson et al., 2019). The maximum computed water level, velocity, and time wet per event and per grid cell were stored. Each storm is ranked, gives the same frequency resulting in an estimate of the probability of m/(n+1) in which m is the ranking and n is the number of years, here

31 (i.e., Weibull plotting position; Weibull, 1939). TC probability per simulation is directly based on the JPM input dataset and the probability estimated by summing the discrete set of storm values.

To combine ETC and TC runs, we first determined the extreme value distribution for high water per grid cell for ETC and TC runs separately. For the three CMIP6 models, we determined the extreme value distribution per model and used the ensemble mean as the estimate for ETC. Afterward, the extremes were combined by taking the inverse of the sum of the TC and ETC yearly exceedance frequency. See, for example, Dullaart et al. (2021) for more information. For given high water, we calculated its return period as follows:

$$\boldsymbol{RP}(\boldsymbol{x}) = \frac{\mathbf{1}}{\frac{\mathbf{1}}{\boldsymbol{RP_{ETC}}(\boldsymbol{x})} + \frac{\mathbf{1}}{\boldsymbol{RP_{TC}}(\boldsymbol{x})}} \qquad \text{Equation 3}$$

where *RP* is the return period in *x* years of high water. RP_{TC} and RP_{ETC} refer to the return period of the TC and ETC water level at the same value of water level. Examples of the probability of high water levels by ETC, TC and jointly for six stations through the domain can be found in the Appendix (Figure 15). No storm conditions were based on a simulation with a spring-neap tidal cycle of 30 days. During this stimulation, we included a baseflow from the rivers but excluded the effects of waves or rainfall. No-storm simulations were included to provide an estimate of nuisance flooding.

Simulation periods and computational expense

We made flood predictions for two time periods: historical (1980-2018) and future projection (2020-2050).

For validation of the model skill, historical conditions were simulated for 1980–2018. First tidal conditions were simulated and compared to NOAA and XTide stations across the U.S. Southeast. This simulation is based on a 365-day-long simulation without meteorological conditions and baseflow discharge rates for the year 2016. Secondly, 198 historical storms were simulated to assess model skill in reproducing extreme water levels. Thirdly, a more in-depth analysis of Hurricane Florence (2018) was performed.

Flood hazard, impact, and risk computations were performed for 2020–2050 using CMIP6 ETC storm events outlined above and TCs from the USACE-JPM method. Additionally, all ETC and TC model simulations were repeated for seven SLR scenarios: 0-, 0.25-, 0.50-, 1.00-, 1.50-, 2.00- and 3.00-meter compared to the year 2005. These scenarios cover the range of plausible sea level projections for the U.S. Southeast through 2100, as reported by Sweet et al. (2022).

Model runs were performed on the Deltares Netherlands Linux-based High-Performance Computing platform using 54 Intel Xeon CPU E3-1276 v3. On average, a 7-day simulation (typical duration for an individual event) took about 41 minutes on a single core. Running all 80,000 events (all TCs + ETCs for seven SLR scenarios) took 31 days.

Model skill

To quantify the skill of the model, several accuracy metrics were calculated: model bias, mean-absolute-error (MAE; Equation 5), root-mean-square-error (RMSE; Equation 6) and unbiased RMSE (uRMSE; RMSE with bias removed from the predicted value)

$$MAE = \frac{1}{N}\sum(|y_i - x_i|) \qquad \text{Equation 4}$$

$$RMSE = \sqrt{\frac{1}{N}\sum (y_i - x_i)^2}$$ Equation 5

where N is the number of data points, y_i is the i-th predicted (modeled) value, x is the i-th measurement.

Results

Validation

Tidal validation

Model skill in reproducing tidal amplitudes and phases is assessed at 24 NOAA stations and 56 XTide stations across the area of interest and presented in Figure 2 and Table 3 in the Appendix. The model framework can reproduce tide with a median MAE of 8.3 cm and a median RMSE for high water of 9.9 cm (median computed over the different stations). Across the region, MAE is typically lower than 20 cm (80% of the stations). The most significant model error is shown at Savannah, Ga. (MAE of 32 cm). The model error generally increases farther away from the ocean boundary in narrow estuaries and harbors. The model-computed tidal amplitude at these locations is typically underestimated compared to observations. We hypothesize that the underestimation of tidal amplitudes has to do with the a) SFINCS model resolution and b) high roughness values from land may be mapped to the channel in some locations due to the coarse resolution of the land cover map.

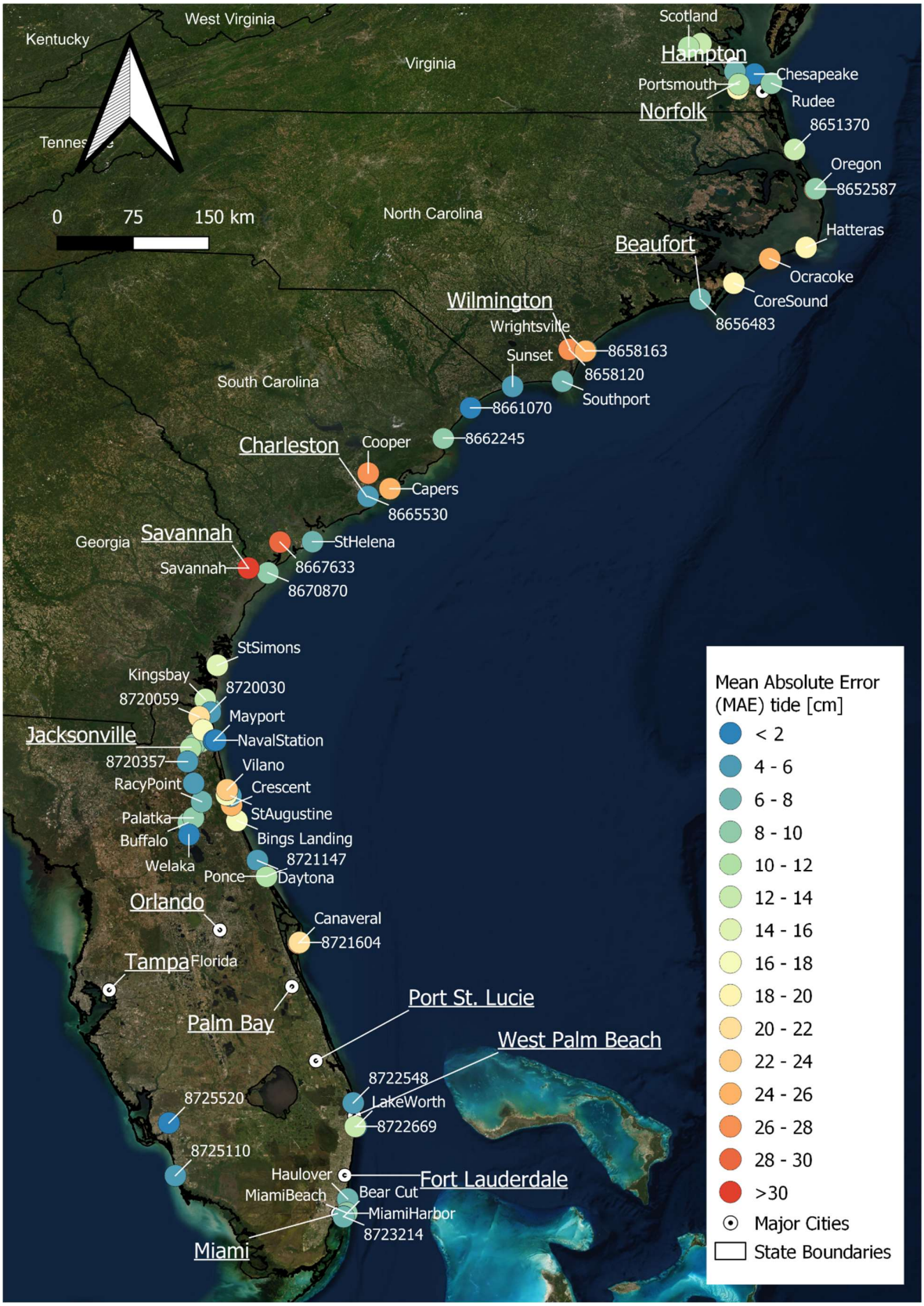

Figure 2. Overview of the Mean Absolute Error (MAE) of tidal water levels at 24 NOAA stations (depicted with station ID) and 68 XTide stations (shown with names) across the study area. For more detailed information on the model skill is

provided in Table 3. Several major city names are presented to orient the reader. © Esri, DigitalGlobe, GeoEye, i-cubed, USDA FSA, USGS, AEX, Getmapping, Aerogrid, IGN, IGP, swisstopo, and the GIS User Community.

Storm validation across the region

Four examples of time series of modeled and observed water levels are presented in Figure 3 for large historical hurricanes for stations from north to south: Irene (2009), Hugo (1989), Matthew (2006) and Wilma (2008). Observed and modeled water levels and tides are shown. Tides are based on astronomical components. The tidal component of the water levels visually match the observations well before the hurricane arrival, except for Money Point, Va. (#8639348). At this station, there is an underestimation of the tidal amplitude, and the tide arrives too late (i.e., overestimating phase). The lower skill for tidal modeling at #8639348 can also be seen in Table 3. The peak water levels are particularly skillful. Computed NTR is also found to match well with the observations since the median MAE increased from 8.3 cm for tide only to 11.9 cm for the water level signal over all storms.

The accuracy of the proposed model framework is presented in Table 1 and Figure 4. Model skill is good, with a median MAE between 8 and 20 cm (25-75 percentile). However, biases per station do exist. For example, Duck, N.C. (#8651370), has a median bias of +25 cm, while I-295 Bridge (#8720357) has a median bias of -19.2 cm. We hypothesize that Duck's overestimation is driven by the inclusion of an open-coast wave setup, which is not measured at the NOAA station (see Parker et al., in review). On the other hand, the underestimation at I-295, being situated inland along the St. John's River, might be driven by an underestimation of pluvial/fluvial processes or by underestimation of tide.

Table 1. Overview of skill scores (mean-absolute-error; MAE, unbiased root-mean-square error; uRMSE and bias) for 24 NOAA observations across 198 events from 1980-2018. The number of storms simulated is listed as 'n'. Skill scores are in cm and computed as the median over the storm events (first value) and the standard deviation is presented as the (second value).

IDcode	Name	n	MAE [cm]	uRMSE [cm]	bias [cm]
8638610	Sewells Point	84	11.7 ± 4.4	10.6 ± 1.6	-8.0 ± 8.4
8639348	Money Point	52	22.2 ± 3.5	20.2 ± 2.7	-15.0 ± 6.9
8651370	Duck	84	29.0 ± 10.9	22.5 ± 5.1	25.2 ± 13.5
8652587	Oregon Inlet Marina	60	14.7 ± 5.7	9.6 ± 3.5	-13.8 ± 7.2
8656483	Beaufort	84	9.7 ± 3.1	9.4 ± 2.8	-2.5 ± 7.3
8658120	Wilmington	68	23.9 ± 4.4	26.3 ± 3.7	-3.0 ± 13.6
8658163	Wrightsville Beach	45	17.7 ± 8.3	12.8 ± 4.7	16.2 ± 9.7
8661070	Springmaid Pier	68	14.5 ± 6.6	13.8 ± 4.1	11.3 ± 9.5
8662245	Oyster Landing	25	10.5 ± 2.8	11.2 ± 2.2	-0.5 ± 6.4
8665530	Charleston	69	12.1 ± 4.2	11.0 ± 2.8	-8.5 ± 8.4
8667633	Clarendon Plantation	16	41.4 ± 7.8	47.1 ± 8.3	-11.9 ± 7.0
8670870	Fort Pulaski	86	14.4 ± 3.3	14.9 ± 3.0	-3.1 ± 8.4
8720030	Fernandina Beach	50	10.2 ±4.8	10.2 ± 4.1	-1.4 ± 9.1
8720145	Edwards Creek	7	14.6 ± 1.9	14.2 ± 1.9	-4.9 ± 8.5
8720218	Mayport	34	8.6 ± 4.2	9.0 ± 3.3	-0.8 ± 8.5
8720357	I-295 Bridge	30	17.6 ± 7.1	7.0 ± 2.7	-19.2 ± 12.4
8721147	Ponce De Leon Inlet	7	6.6 ± 2.5	6.2 ± 1.5	4.4 ± 3.6
8721604	Trident Pier	29	10.5 ± 3.4	11.0 ± 1.6	2.7 ± 8.1
8722548	Palm Beach	7	11.6 ± 4.2	12.2 ± 5.5	4.8 ± 7.6
8722588	Port of West Palm Beach	7	10.3 ± 6.3	13.3 ± 6.9	10.3 ± 7.9

8722669	Lake Worth ICW	7	12.4 ± 5.2	11.1 ± 4.7	12.4 ± 6.8
8723214	Virginia Key	39	8.8 ± 4.7	7.8 ± 2.9	4.3 ± 8.8
8725110	Naples	57	8.8 ± 3.5	8.6 ± 3.1	-1.9 ± 8.0
8725520	Fort Myers	59	8.2 ± 4.3	7.7 ± 2.7	-3.2 ± 8.0
	Median		**11.9**	**11.1**	**-1.6**

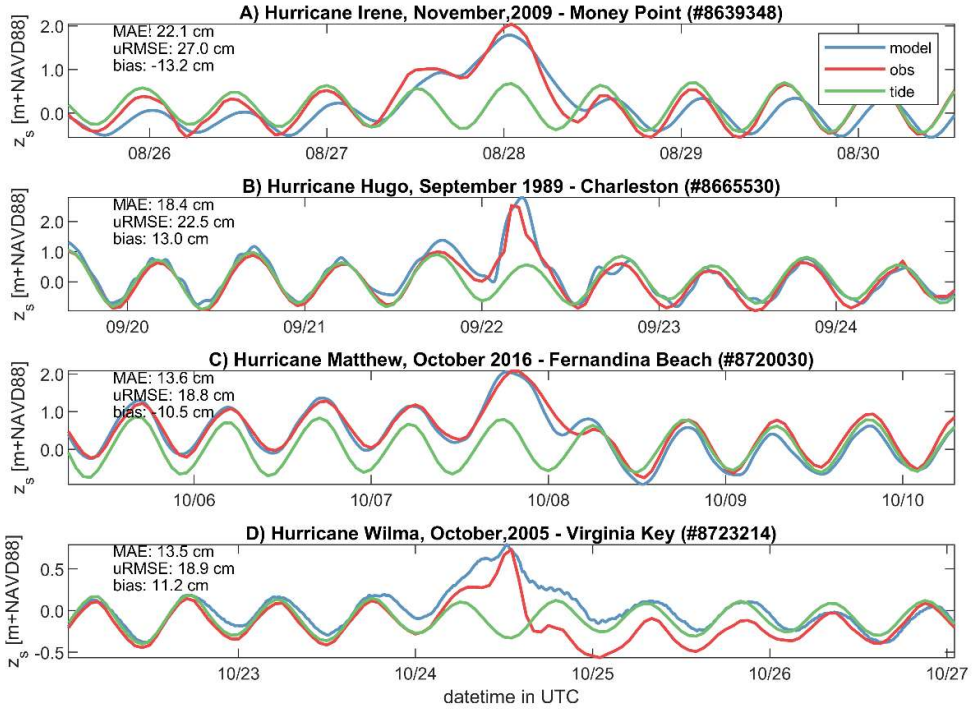

Figure 3. Time series of observed (red), computed (blue), and tidal (green) still water level for four events across the area of interest. Panel A depicts Hurricane Irene (2009) in time series at Money Point, Virginia. Panel B shows Hurricane Hugo (1989) at Charleston, South Carolina, C Hurricane Matthew (2016) at Fernandina Beach, Florida, and D depicts Hurricane Wilma (2005) at Virginia Key, Florida. Stations are listed from north to south. Skill scores are presented in the top left corner.

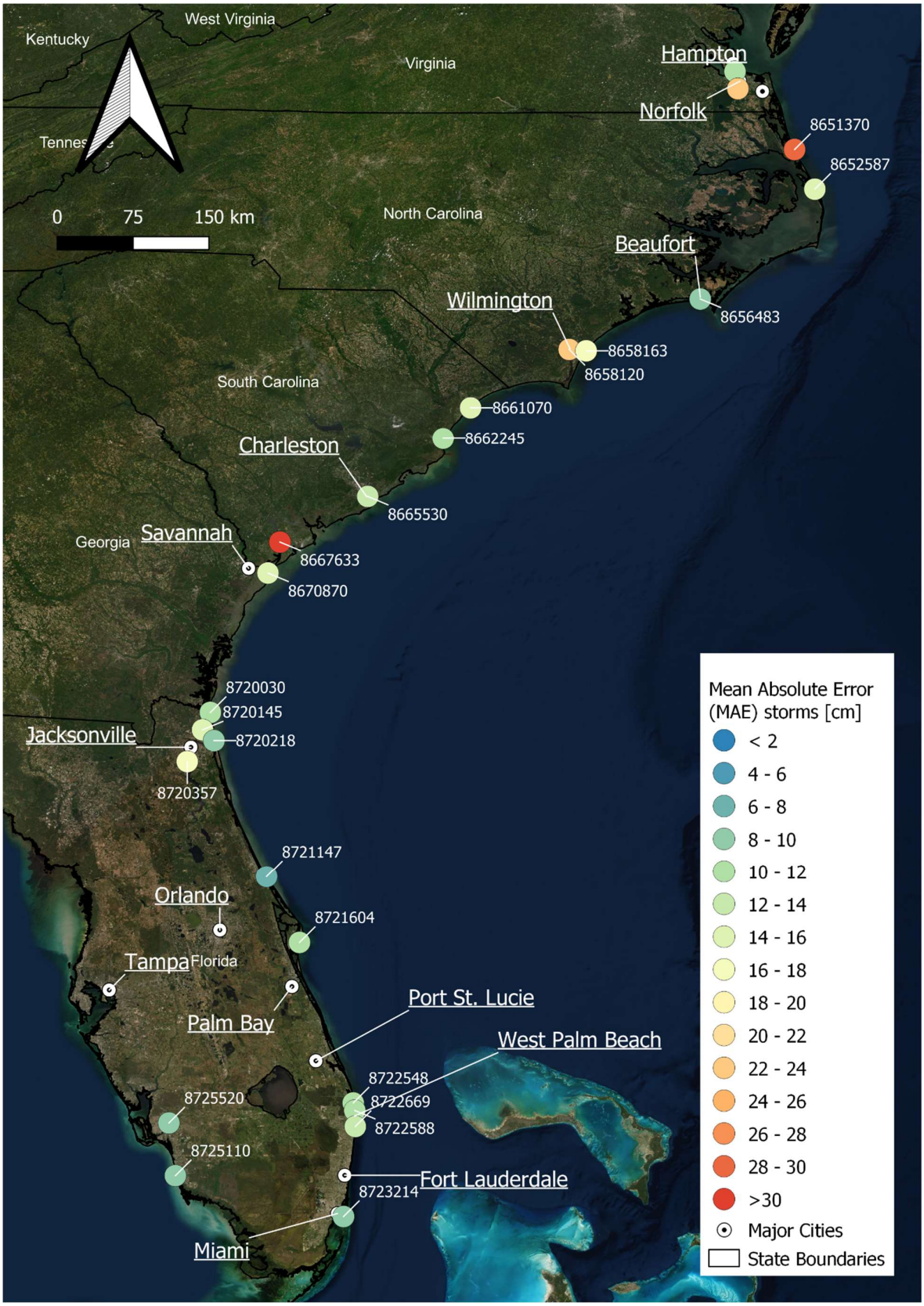

Figure 4. Overview of the median Mean Absolute Error (MAE) of storm water levels at 24 NOAA stations (depicted with station ID) across the study area. For more detailed information on model skill, refer to Table 1. Several major city names

are presented to orient the reader. © Esri, DigitalGlobe, GeoEye, i-cubed, USDA FSA, USGS, AEX, Getmapping, Aerogrid, IGN, IGP, swisstopo, and the GIS User Community.

Hurricane Florence

In this section, we validate the SFINCS model setup for Hurricane Florence (2018). The spatial extent of this more detailed validation covers about 500 km alongshore centered around Wilmington, N.C., where Florence made landfall, and includes all data available within the cross-shore extent of the SFINCS domains (~100 km). Figure 5A shows the orientation compared to the rest of the study area including the track of Florence. Merged model results for SFINCS domains #4 and #5 were used in this section. Figure 5B presents the stations used for the more in-depth validation of Florence, a combination of permanent NOAA gauges and USGS deployed rapid deployment gauges and high water marks (HWMs; U.S. Geological Survey, 2021). The validation will focus first on reproducing six time series in the area, after which the HWMs are discussed. These time series are randomly chosen across a range of stations to show coastal, riverine, and mixed locations with various degrees of model skill.

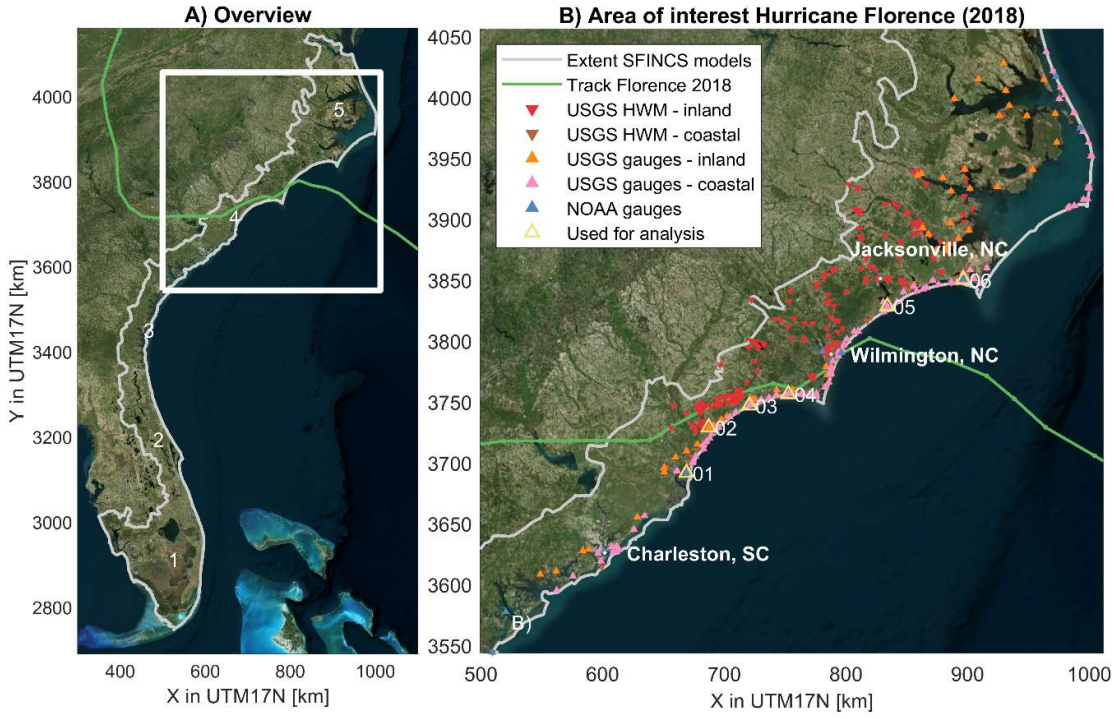

Figure 5. Observational data and model extent for the detailed validation of Hurricane Florence (2018). Panel A: overview figure for the entire study area showing the five different SFINCS (Super-Fast INundation of CoastS) domains, the track of Hurricane Florence (green) and the area of interest Panel B: USGS stations used for the validation of Hurricane Florence model results. USGS gauges have been divided into coastal (pink) and inland (orange) locations based on the classification given when the data were released. Gauges and high water marks (HWM) are marked, respectively, with upward-pointing and downward-pointing triangles. The best track is based on International Best Track Archive for Climate Stewardship (IBTrACS; Knapp et al., 2010).The coordinate system of this figure is WGS 84 / UTM 17 N (EPSG 32617). © Microsoft Bing Maps.

The time series of the water levels for six gauges around the landfall of Hurricane Florence are shown in Figure 6. The first gauge shows Oyster Landing, N.C. (#8662245). At this station, the model reproduces the tide well (as shown in previous sections). Oyster Landing is located southwest of the location of landfall, which explains the decrease in water-levels (setdown) caused by offshore directed wind after landfall of the TC. The second gauge, USGS SCHOR14330, located in a local creek and about 1 km from the shoreline, mainly shows the impact of rainfall runoff, albeit slightly influenced by tides. The model can reproduce both signals. Gauges 3, 4, and 6 show a similar pattern

of tidal oscillation with a slight increase in mean water level with the hurricane's landfall. These temporarily placed gauges were only partially inundated, so they only provided a signal to compare the model with at higher water levels. Gauge 5 was in a salt marsh near the town of Sneads Berry, N.C., close to the New River estuary. The observations show a tidally influenced riverine behavior where the water level rises due to rainfall until several days after landfall, after which time the water level slowly falls again. The model underestimates the peak of the water level, possibly due to the underestimation of the TC precipitation boundary condition. Moreover, the model drains too quickly compared to observations, which could be caused by hydrological processes such as infiltration via the Curve Number method or underestimation with friction.

High water marks are compared to modeled water depth and water level in Figure 7. A clear flooding pattern of the hinterland is both computed and observed (Figure 7A). The model underestimates the HWM (Figure 7B). Based on the division between coastal and riverine points, the underestimation is already present in the coastal points (30 cm); however, the bias reaches 91 cm for the riverine points. These biases affect the model skill, resulting in a MAE for all the points of 69 cm. A similar result is shown for the linear regression fit (green line), which has an offset that gets worse with higher water levels. We hypothesize that this underestimation is driven by a difference in modeled (input) and actual precipitation and river discharge. This situation would explain why the time-series model skill is higher than HWM skill.

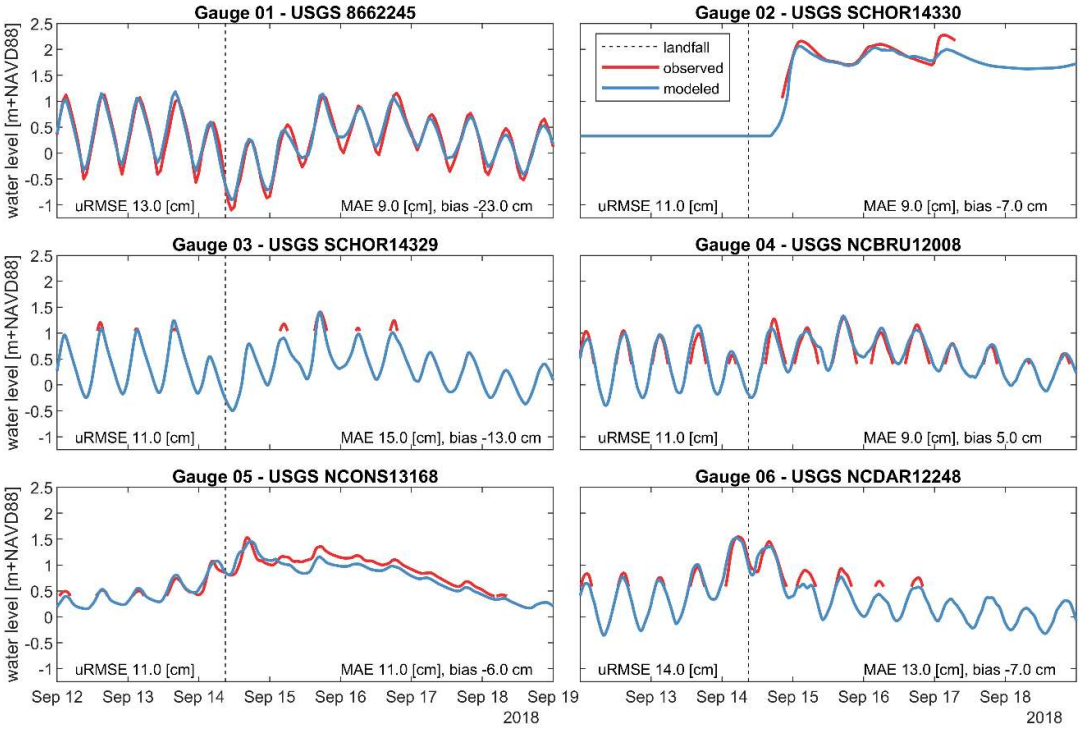

Figure 6. Water level time series as observed (red) and modeled (blue) during Hurricane Florence (2018). Dashed black line is moment of landfall. The location of the six gauges is shown on the map in Figure 5 and stations are listed from west to east.

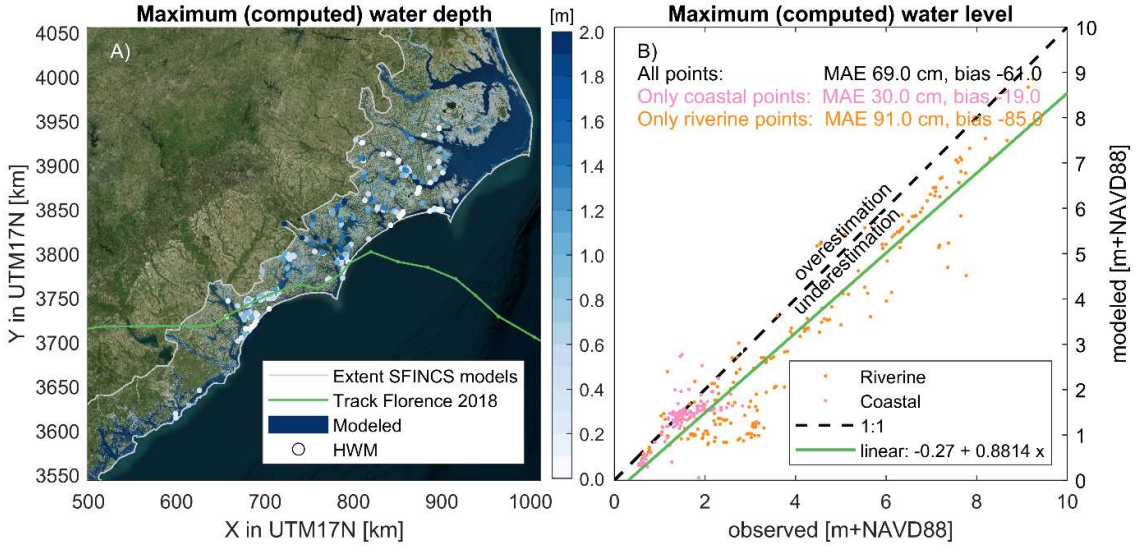

Figure 7. Validation of the maximum water depth and level for Hurricane Florence (2018). Panel A: maximum water depth with high water marks (HWMs; circles) compared to spatial color for model. Panel B: maximum water level for the same HWMs. Different colors represent either coastal (pink) or riverine (orange) points. 'Linear' is a least-squares linear fit on all the data points and shows tendency for underestimation of the modeled HWM (negative bias) that increases with water level. Note the increasing dealignment between the green line and dashed black line. Model estimates of extreme water levels have substantial scatter and bias which increases with water level. The latter explains the higher error for riverine versus coastal points. The coordinate system of this figure is WGS 84 / UTM 17 N (EPSG 32617). © Microsoft Bing Maps.

Projected flood hazards and impact

Flood hazards

While flood hazards are calculated on a high detail level (tens of meters) for over 1000 km of coastline, for clarity we present these for a limited region around Charleston, S.C., only as an example of the output (Figure 8). Panels A and B show shows the water level (A) and Panel B the water depth, both (B) for a return period of 50 years and the SLR scenario of 100 cm. Panel C presents the range of flooding for progressively larger events for the SLR scenario of 100 cm with colors indicating a flooded grid cell and associated lowest return frequency. Finally, panel D presents progressing effects of sea level for a 50-yr storm. The color represents which SLR scenario, given a 50-year event (2% chance per year), results in flooding. Data for all return periods and SLR scenarios can be accessed via Barnard et al. (2023a; b).

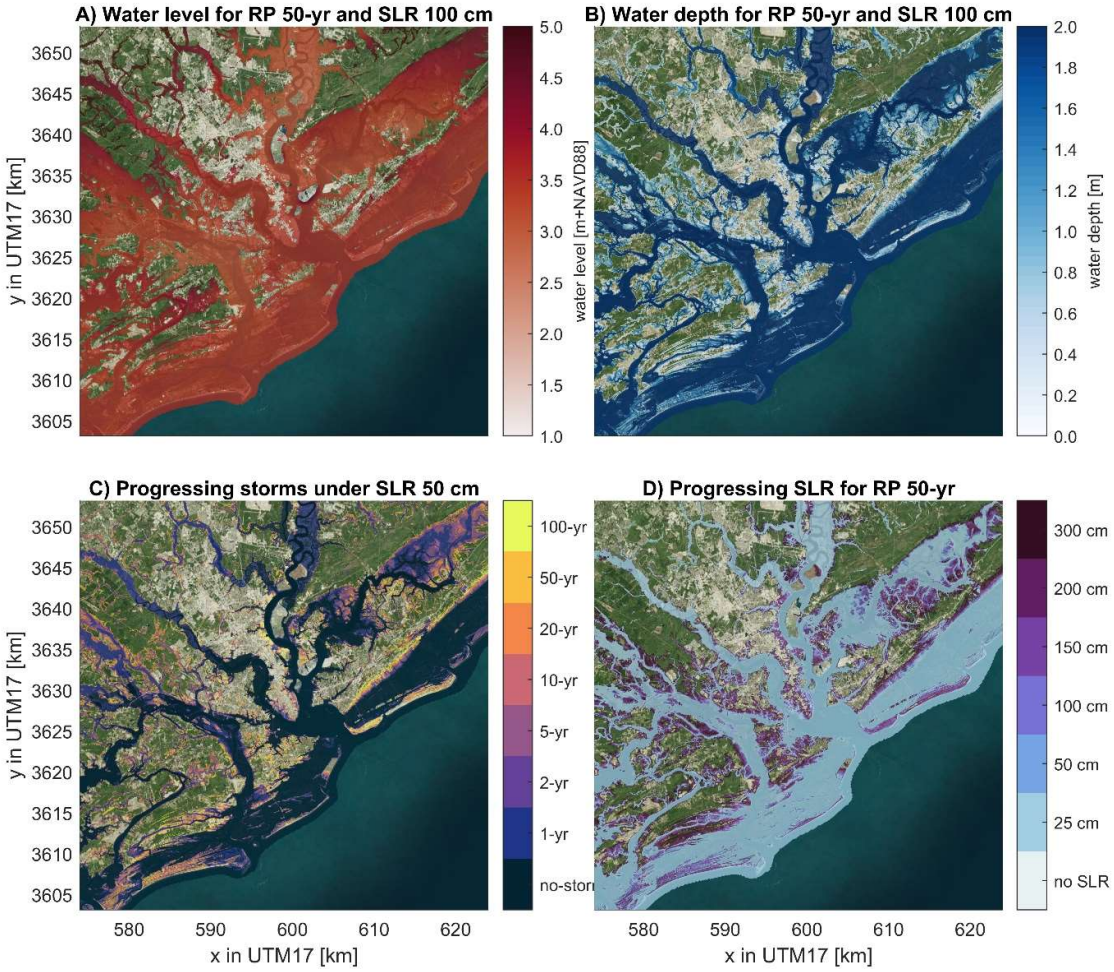

Figure 8. Example output for Charleston, S.C.. Panel A: Water level for a 50-year return period storm in combination with a 100 cm SLR. Panel B: Water depth 50-year return period storm in combination with a. Panel C: progressing flood extent for different storm frequencies for a SLR scenario of 100 cm. Panel D: Progressing flood extent for different SLR scenarios for a 50-year return period. The progressing flood extent (C and D) shows with which lowest storm frequency or sea level rise scenario the area gets flooded. The coordinate system of this figure is WGS 84 / UTM 17 N (EPSG 32617). © Microsoft Bing Maps.

A regional analysis of flood-hazard area (minimum threshold water depth of 10 cm) over the entire U.S. Southeast is shown in Figure 9. Only grid cells with a bed level above NAVD88 + 1 m are considered, to exclude low-lying flooding of natural systems. The area of interest is defined as the Low Elevation Coastal Zone above NAVD88 +1 m. Flood hazards can occur during no-storm conditions (i.e., flooding during regular tides together with SLR, consider here as nuisance flooding, shown in panel A) or storm conditions with a specific return period (panel B). A relatively small area currently gets flooded under regular (non-storm) conditions, representing ~2,000 km^2 or 1% of the area of interest. This flood hazard area increases significantly with SLR. The increases with SLR are initially small but increase at more than a linear rate. For example, an increase of the mean sea level from the current level to 50 cm increases the non-storm flood hazard by ~560 km^2(+26%). The same mean sea level increase from 100 to 150 cm results in an increase of flooded area by >4,200 km^2 (+750% increase). In other words, increasing sea level inundates disproportionally more and more area. Storm hazards increase with return period and rising sea level (Figure 9, panel B) . Yearly storm events without SLR (SLR of 0 m) flood around 13,000 km^2 or 6.2% of the study area and are projected to increase to 8.0 and 11.7% for 100 and 200 cm of SLR, respectively. The 100-year flood event, without SLR, floods almost 4.5 times as much area compared to the annual event. Moreover, Figure 9B shows a well-described phenomenon in the scientific literature (e.g., Vitousek et al., 2017), where, for instance, a 20-year flood hazard at current sea level will, with 200 cm SLR, be the new 3-year event (i.e., decreased return period).

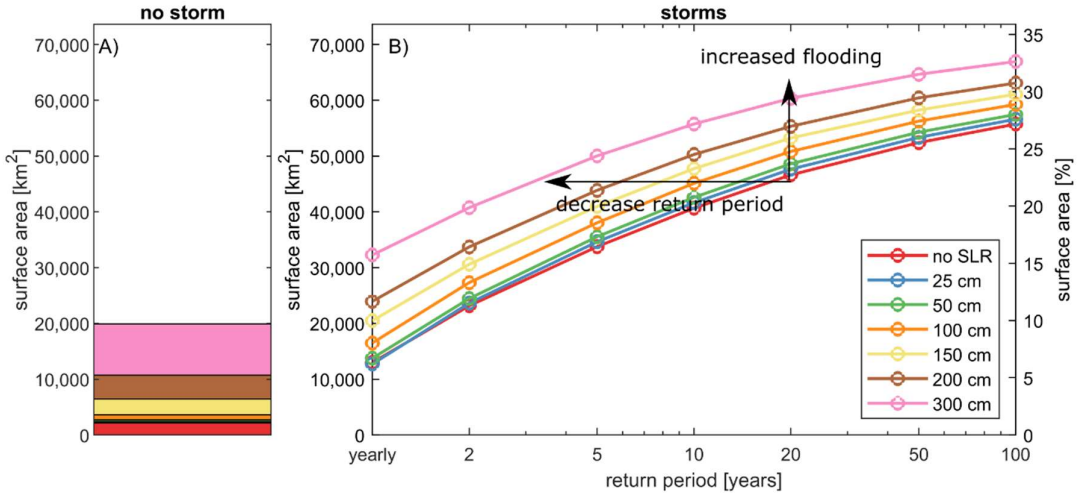

Figure 9. Flood hazard for the no storm (daily; tide-only) condition (left panel A) and storms (right panel B). Color depicts different sea level scenarios of current sea level (red), 25 cm (blue), 50 cm (green), 100 cm (orange), 150 cm (yellow), 200 cm (brown) and 300 cm (pink). Note that A and B share the same y-axes. For absolute numbers use the left y-axis and for a relative of the total the right y-axis. Hazards increase with increasing SLR scenarios, which means that the same area is flooded with lower return periods and that the same storm return period gets more severe. The relative increase in surface area is larger for lower return periods than for higher return periods and increase more than linear for higher SLR scenarios.

Analyzing the entire area of interest together allows for the quantification of flood impact in number of people affected for both non-storm (i.e., nuisance flooding; Figure 10A) and storm conditions (Figure 10B). Model results indicate that on average 150,000 people are currently affected yearly by compound flooding in the coastal zone. People are impacted as a function of the hazard (water depth), exposure (where people are located), and vulnerability (depth-damage curve; see also Materials and Methods section). This increase grows to 2,210,000 for a 100-year event (1% chance). That is an increase from 1 to 14% of the total population of the area of interest. A 100-year flood impact today will be a yearly impact with a 200 cm SLR. Moreover, the 20-year impact increases from 1.4 to 3.3 million people for 150 cm of SLR. This is an increase of 132% and is substantially higher than the increase in flood hazard for the same return period and SLR scenario (14%). Also, the number of people expected to be negatively affected by non-storm conditions (i.e., nuisance flooding) is likely to increase to almost 3 million for 300 cm of SLR.

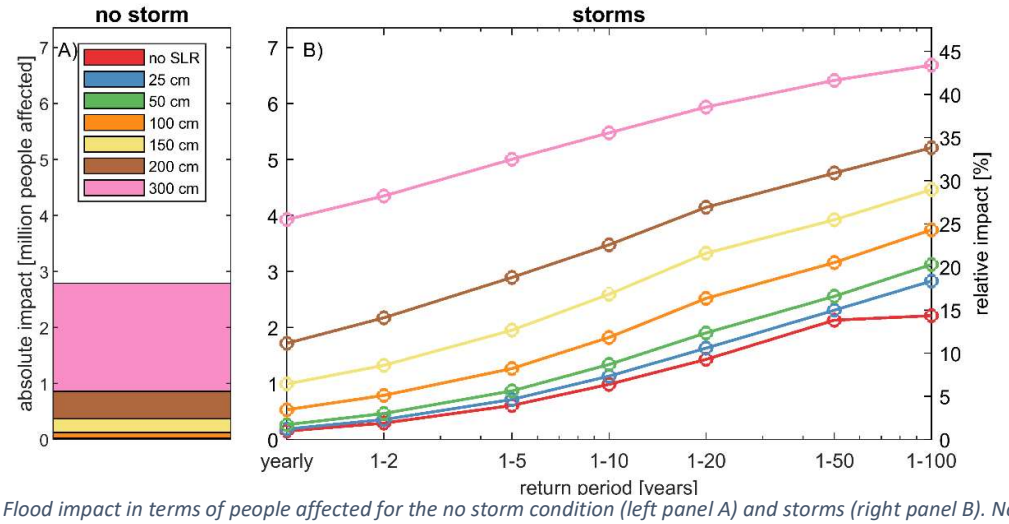

Figure 10. Flood impact in terms of people affected for the no storm condition (left panel A) and storms (right panel B). Note that A and B share the same y-axes. For absolute numbers use the left y-axis and for a relative of the total the right y-axis. Color depicts different sea level scenarios of current sea level (red), 25 cm (blue), 50 cm (green), 100 cm (orange), 150 cm (yellow), 200 cm (brown) and 300 cm (pink). Impacts increase with increasing SLR scenarios and have a large relative increase compared to hazards (Figure 9).

Flood impacts per return period can be integrated over frequency to provide an estimate of annual risk. This process, which will be referenced throughout the rest of the paper as (absolute) flood risk, is used in generating the results shown in Figure 11 through Figure 14. The non-storm scenario is not included in the flood risk estimate. In particular, we integrated the affected people per storm frequency and compute the Expected Annual Affected People (EAAP; Giardino et al., 2018). Figure 11 presents the EAAP as a function of SLR for the 14 most populous counties in the area of interest. The most considerable contribution of the total compound flood risk is for the three southeast Florida counties of Miami-Dade, Broward, and Palm Beach Counties (i.e., greater Miami metropolitan area), which comprise 62-72% of the total EAAP.

Similar to flood hazards, there is a stronger than linear increase of impact of flood risk as a function of SLR. The first 50 cm SLR results in an increase in EAAP from 480,000 to 700,000 people. That is an increase of 220,000 people (+45%). SLR scenarios of 100, 150, and 200 cm result in increases of 360,000, 530,000 and 840,000 EAAP (+119, +240, and +413% or fourfold increase).

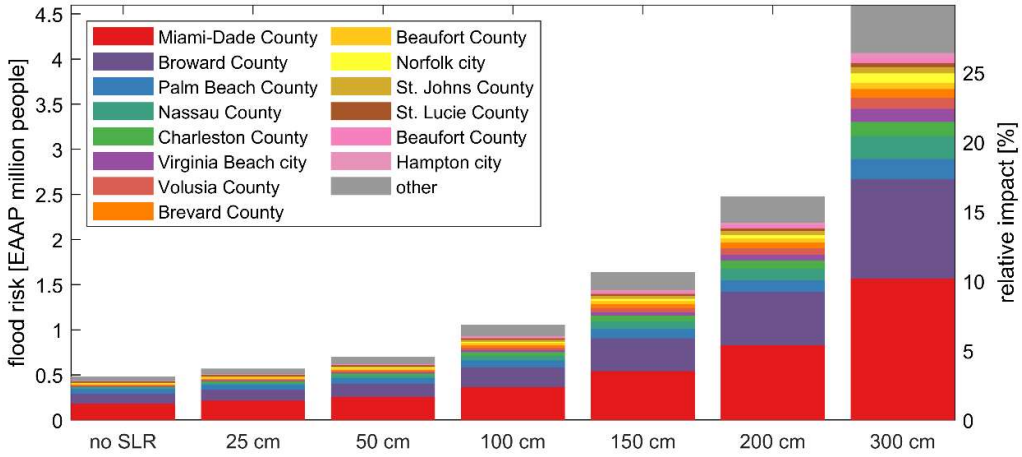

Figure 11. Flood risk in Expected Annual Affected People (EAAP) as a function of sea-level-rise (SLR) for absolute numbers (left y-axis) and percentage of total (right y-axis). Color depicts the top affected 14 counties, including the 15th color for all the other counties (gray). EAAP increases strongly with SLR, and the Florida's Miami-Dade, Broward, and Palm Beach Counties account in absolute as relative terms for the largest EAAP.

Absolute flood risk or EAAP strongly follows exposure; thus, densely populated areas generally have the most significant flood risk in this analysis. Relative flood risk can be computed dividing the EAAP by the county's total population (Figure 12). Vulnerable counties such as Miami-Dade and Broward Counties are both populous and have a high relative flood risk. However, a county like Poquoson in Virginia does not show up in the previous (absolute) analysis but does in terms of relative risk because a high percentage of the population would be exposed to flooding (Figure 12). In a situation without SLR, these communities can be negatively affected during rare but severe storms (e.g., 100-year events). For the example of Poquoson County, with 1.6-meter of SLR, what is currently a 100-year flood impact event will become the new yearly event with dire consequences regarding relative flood risk.

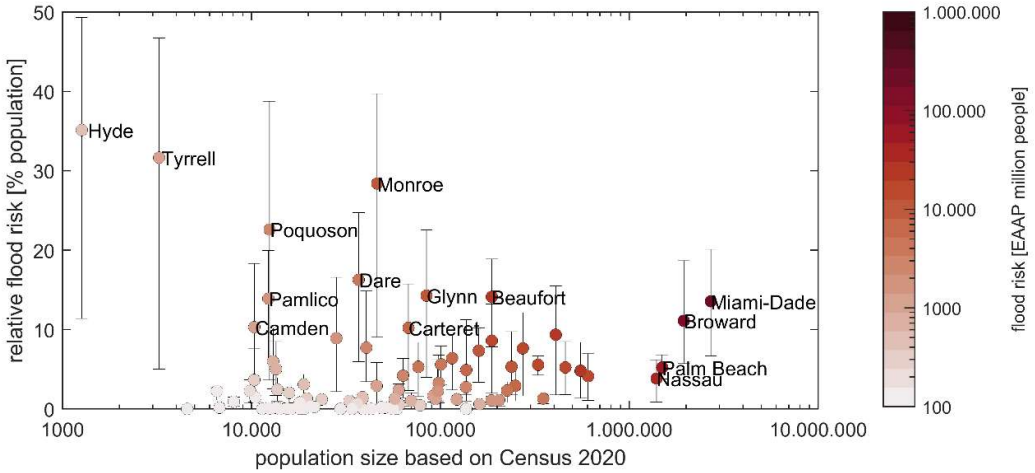

Figure 12. Relative flood risk as a function of population size for a SLR projection of 1 m color-coded in Expected Annual Affected People (EAAP). The bar shows the change from the current sea level to 1 meter (lower value) and the increase from 1 to 2 meter. Several smaller, less populous counties have the highest relative risk of the area.

Relative flood risk provides a framework to identify when significant proportions of counties will start to face negative consequences because of SLR. Figure 13 shows the relative flood risk per county for the different SLR scenarios analyzed (25 cm SLR results are not shown, for conciseness of the figure). Higher sea levels result in more relative risk. In particular, only one county (Hyde County) has a relative compound flood risk greater than 10% for the current sea level. This value is expected

to increase to 12 counties for a SLR of 100 cm and 41 for 300 cm for a total of 94 counties analyzed. Similarly, no county has a 20% or higher flood risk for the current sea level (see also Figure 12). With 100 cm of SLR, four counties (Poquoson, Tyrrell, Monroe, Hyde) will have this level of relative flood risk, and this increases to 29 counties with 300 cm of SLR. Note a low risk does not mean that a county cannot be impacted by floods. It means there is a lower likelihood that a large percentage of the county's population is negatively impact by flooding.

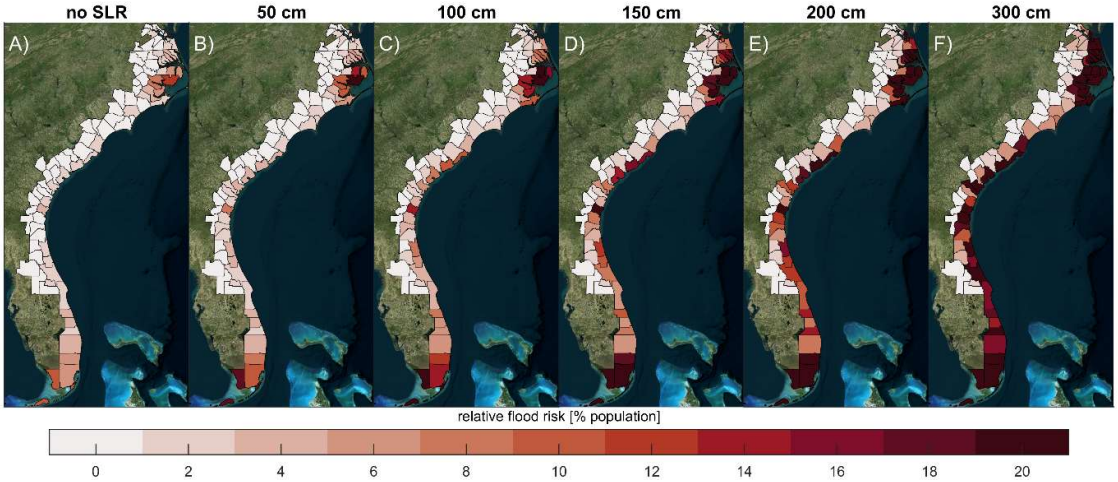

Figure 13. Color-coded relative flood risk per county as a function of sea-level-rise (SLR). Different panels (A-F) represent different SLR scenarios (no SLR to 300 cm). 25 cm SLR results are not shown, for conciseness of the Figure. Relative flood risk is projected to increase with SLR. The coordinate system of this figure is WGS 84 / UTM 17 N (EPSG 32617). © Microsoft Bing Maps.

Tropical versus extratropical

The relative portion of TCs, ETCs, or either physical driver can be determined by the differences between the combined results and the TC- or ETC-only results for flood hazards (Figure 14A; flooded area), flood impact (Figure 14B; impacted people), and flood risk (Figure 14C; EAAP). For example, the combined flood hazard zone of the whole area with 100 cm of SLR and an annual return period is 16,489 km^2. Only considering TCs results in a hazard area of 7,360 km^2 and ETCs alone gives 9,201 km^2. Combining the TC-only and ETC-only areas gives an area larger than the combined flood hazard zone by 72 km^2, indicating the portion of the combined flood hazard zone that can be flooded by either driver (0.4%). Of the combined flood hazard zone, the portion that is due to ETCs-only is thus 55.4% (9,129 km^2), and the portion due to TCs only is 44.2% (7,288 km^2). Therefore, we estimate that ETCs dominate the annual flood hazards compared to TCs (division is 55.6% ETC and 44.4% TCs). The division between TCs and ETCs are computed by dividing the area flooded uniquely by ETCs compared to the total area that is uniquely flooded by ETC and TCs.

Flood hazards (Figure 14A), regardless of the driver, increase considerably as a function of the return period from ~16,500 km^2 for annual return period (8% area) to ~60,000 km^2 (29% area) for the 100-year event. For higher return periods, TCs drive an increasingly larger share of the division. For example, a 2-year event (50% annual probability) is 47.2% driven uniquely by TCs versus 24.5% uniquely by ETC and 28.3% by either driver. This percentage of uniquely flooded areas results in a breakdown of 66% for TCs and 34% for ETCs[3]. This breakdown increases to 96% for TCs and 4% for ETCs for the 100-year event (1% annual probability). The increasing dominance of the third category, either physical driver (Figure 14 – blue colors), is due to the binary nature of flood hazards (i.e., wet or dry). In other words, low-lying areas will get flooded for the most extreme events regardless if the driving force is a TC or ETC. The analysis only reveals if areas get flooded uniquely by TCs or ETCs. We

[3] 12,883 km^2 uniquely flooded by TCs versus 6,686 km^2 by ETCs results is 12,883 / (12,883+6,686) = 66% TC and 34% ETCs division.

apply the ratio to establish the division between ETC and TC. For a visual impression of this analysis, see in the Appendix a detailed breakdown for Charleston, S.C., flooding with annual frequency, 10-year, 100-year (Figure 16).

A similar trend emerges for the flood impacts (Figure 14B). For a SLR scenario of 100 cm, we estimate that ~530,500 people (3.4%) are negatively affected annually by flooding. This impact increases to almost 3,743,000 people (or 24.3% of the population) for the 100-year event. The annual impact is about 22.7% uniquely driven by TCs, 42.8% by ETCs, and 34.5% by either driver. In other words, ETCs result in almost twice the amount of negative impact with a yearly frequency based on the division estimate (division TC/ETC 35-65%). However, for the 100-year event, 58.3% is driven by TCs versus 2.0% by ETCs and 39.8% by either driver (i.e., 30x more TC-driven impact). The lack of linear correlation between hazards and impacts is noteworthy.

Regarding flood risk (Figure 14C), TCs generally dominate over ETCs. For the current sea level, 52.2% of the flood risk is uniquely related to TCs. In comparison, 24.1% is related to ETCs and 23.7% to either driver. In other words, TC-induced flood risk is about twice that of ETCs based on the division TC/ETC. This distribution of risk decreases to 17.3% TCs, 14.0% ETCs, and 68.7% for either driver for the 300 cm SLR scenario. Higher SLR scenarios result in more and more flood risk regardless of the ETCs or TCs. Moreover, the contribution of TCs to compound flood risk decreases from 70 to 55% from no SLR to 300 cm (or 30% and 45% ETCs).

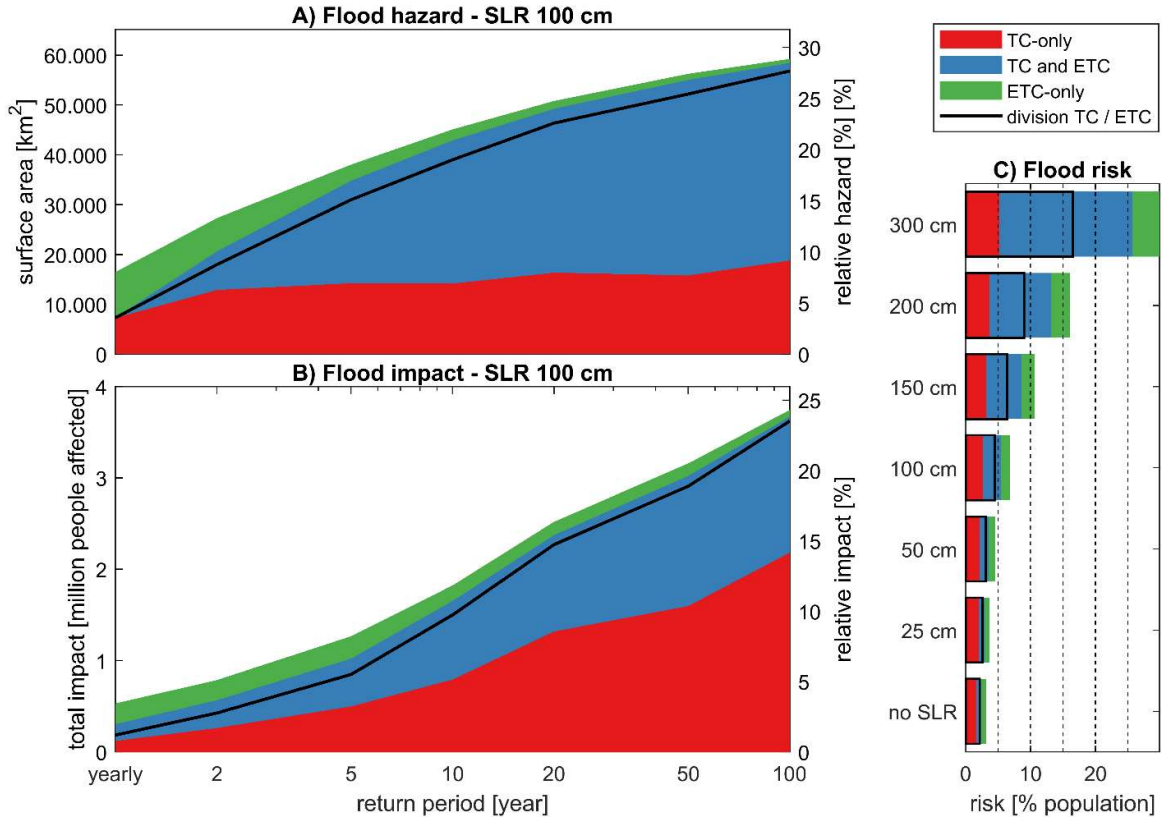

Figure 14. The division TC/ETC (black line) and contribution of TC-only (red) versus ETC-only (green) or either (blue) for compound flooding. Panel A. Flood hazard as a function of return period for SLR scenario of 100 cm. Panel B. Flood impact as a function of return period for SLR scenario of 100 cm. Panel C. Flood risk in EAAP for different SLR scenarios. The contribution of TCs increase with return period for both hazards and impacts but decreases for flood risk as function of SLR.

Discussion

The validation shows that our workflow and the developed five SFINCS domains can skillfully reproduce tidal (median MAE 8.3 cm; Figure 2) and coastal extreme water levels (median MAE 11.9 cm; Figure 4). We hypothesize this model skill has been achieved by 1) nesting the overland flow domains into large-scale hydrodynamic and wave models that provide statistically corrected boundary conditions and 2) including relevant bathymetry features. Computational efficiency was prioritized to allow for the deterministic computation of flood hazards and impacts of thousands of events. Limited computational resources did limit the utilized approach to a relatively coarse model resolution of 200x200 meters in combination with subgrid lookup tables that resolve fine-scale flood features at the resolution of the 1-m Digital Elevation Model. Similar to other approaches (e.g., Volp et al., 2013; Sehili et al., 2014), the subgrid approach substantially reduced computational cost without significant accuracy loss. The underestimation of tides at several stations is likely driven by incorrect friction, as derived from the landcover map, and not a limitation in the subgrid method itself. The accuracy of the boundary conditions could also play a role (see Parker et al. in review). Moreover, as part of sensitivity testing, we found that model skill versus computational cost seems optimal at a model resolution of 200x200 meters. More refined model simulations minimally increased model skill with considerable computational cost. The near-continuous computations allowed for the usage of empirical extreme value statistics on a cell-by-cell basis. This method eliminated the need of fitting statistical distributions that could potentially yield incorrect results when limited data points are presented. The latter mainly occurs for overland compound flooding, where only several (rare) storms result in flooding.

The version of SFINCS applied in this manuscript does not include a stationary wave solver, infragravity waves, sediment transport, or morphology. Wave setup was used at the offshore boundary based on the empirical formula of Stockdon et al. (2006) and presented in Parker et al. (in review). Still, we were not able to assess the accuracy of this correction. A more in-depth validation at a case study site with good observational data might provide insight. The lack of infragravity waves, sediment transport, and morphological change is a limitation since breaches and overtopping are commonly reported during extreme events (e.g., during Hurricane Florence; Biesecker & Kastanis, 2018 or more recently during Ian and Nicole in 2022 season). This restriction would, most likely, result in underestimating the computed flood hazards and impacts. Moreover, in this paper, we have assessed flood hazards and impacts given SLR scenarios but without taking into account morphological and societal changes such as population dynamics. The natural system will respond given changes in climate (Antolinez et al., 2018). For example, shorelines are projected to undergo large recession (e.g., Bruun, 1956; Ranasinghe et al., 2012). Moreover, the U.S. Southeast is projected to continue its economic growth (Hauer, 2019), but any local mitigation and adaptation measures taken will be beholden to the question of how flood hazards and risks develop in the future. These changes are not considered in this paper. Moreover, no validation of the impact computation was performed. Lastly, Lockwood et al. (2022) showed that sea level rise and changes in the meteorological conditions correlate; however, in this paper we have assumed independence to allow for the computation of several sea level rise scenarios under one future projected climate.

Hydrological processes were resolved in this paper by 1) applying the NWM for riverine inflow into the SFINCS domains and 2) computing rainfall run-off by including rainfall and estimating infiltration with the Curve Number method. Validation for Hurricane Florence did show clear observed and modeled inland flooding, including raised water levels in the analyzed time series of observations and model due to precipitation and riverine flow (Figure 7). However, the error in reproducing the HWM with a MAE of 63 cm is much higher than the other errors presented in this paper, but they are in the same order as other Hurricane Florence validations (e.g., Ye et al., 2021 reported an average MAE of 73 cm). In addition, dynamic processes such as groundwater and (managed) urban drainage systems are not included, which could substantially influence results locally. For example,

South Florida is known for its permeable karst substrate in combination with regulated channels, which affects the risk of flooding (Czajkowski et al., 2018; Sukop et al., 2018). Moreover, it is unknown how the assumption of 50% saturation in the Curve Number at the start of each simulation has influenced the results. Continuous, deterministic, simulations could overcome this limitation. Besides these limitations, the SFINCS-based estimate of flood hazards and impacts across the region provides valuable information to coastal managers and policymakers on an unprecedented scale and resolution. In particular, we hypothesize that reported hazard, impact and risk values can always provide relative insights due to the physics-based derivation despite the model error.

The simulation and detailed analysis of both TCs and ETCs allowed quantifying the contribution of tropical and extratropical events. Similar to Dullaart et al. (2021), this paper also found that it is vital to include TCs, especially for infrequent events. Here, we estimate a dominance in TC risk across the study area to be around 55-68%, which is in the same order of magnitude as Dullaart et al. (2021), who provided estimates for storm surge across the globe or Booth et al. (2016) who provided its estimate based observational water level data. A limitation of our study is the record length of 31 years for ETCs and, therefore, implicitly assuming dominance of TCs for higher return periods. However, in this study, we do see that TCs dominate the signal earlier in the frequency range for the Southeast Atlantic Coast. For other areas (e.g., West Coast or New England states), this dominance of TCs is most likely not the case, and another method needs to be explored.

Conclusions

Using a well-calibrated numerical model, we show that predicting both tropical and extratropical cyclones is vital for accurately assessing coastal hazards and impacts. Extratropical cyclones are mainly responsible for frequent flooding events. In particular, we find that for the current sea level, extratropical cyclones contribute to half of the flooded area. However, these events affect almost twice the amount of people compared to tropical cyclones with a yearly frequency. However, tropical cyclones drive the majority of the infrequent flood hazards. For example, for the 100-year event, tropical cyclones contribute ~96% of the flooded area and likely affect 30 times the amount of people. Moreover, we find that tropical cyclones contribute to more than half of the total coastal compound flood risk. The importance of tropical cyclones to compound flood risk does decreases with sea level rise.

The relative impact of annual flood hazards is limited to 6.3% of low-lying areas of U.S. Southeast Atlantic coast at the current sea level. In comparison, 100-year events flood 27.2% of the considered area. With sea-level rise (SLR), flooding increases significantly. In particular, annual hazards increase from 6.3% today to 8.0 and 11.7% with 100 and 200 cm, respectively, of sea level rise. This change makes rare events more severe and decreases the return period for current extreme events. For example, a 100-year flood impact today will be a yearly impact with a 200 cm SLR. Also, flood impacts are projected to have a larger relative increase compared to flood hazards for the same return period and SLR scenario. Flood risk is expected to grow non-linearly from roughly 3.1% (0.5 million people) today to 6.9 and 16.1% (1.1 and 2.6 million people) for 100 and 200 cm, respectively, of sea level rise. Impacts are mainly driven by exposure in the most populous counties in the area (Miami-Dade, Broward, and Palm Beach County together comprise 62-70% of the total risk in the area). However, several smaller, less populous counties have the highest relative risk of the study area compared to the high absolute flood risk for the populated southeast Florida region. This implies that relative risk (people affected divided by the total population in the county) could prove a valuable metric for policy decisions.

While our methodology is targeted at coastal flooding, precipitation and hydrology are included to capture coastal compound flooding. In particular, the model framework developed in this study can skillfully reproduce coastal water levels. Model errors in these areas are driven by errors in tide

(median mean-absolute-error, MAE, 8.3 cm) and storms (median MAE 11.9 cm). As demonstrated in the validation of Hurricane Florence, the model error increased farther inland due to less well-resolved hydrological processes such as rainfall, infiltration, and riverine flow.

Funding

This research was funded by the Additional Supplemental Appropriations for Disaster Relief Act of 2019 (H.R. 2157) for North Carolina and South Carolina and by the Coastal and Marine Hazards and Resources Program for the remaining states, as well as the Deltares Natural Hazards Strategic Research Program.

Acknowledgments

We acknowledge USGS staff contributions on performing a detailed QA/QC procedure on the model results. Moreover, we want to thank Bjorn Robke for Figure 1. José Álvarez Antolínez, Ap van Dongeren, Dano Roelvink, James Shope and Thomas Wahl all provided a review to this paper, which substantially improved this manuscript. The data supporting this paper are available in Barnard et al. (2023a; b). Any use of trade, firm, or product names is for descriptive purposes only and does not imply endorsement by the U.S. Government.

References

Antolínez, J. A. A., Murray, A. B., Méndez, F. J., Moore, L. J., Farley, G., & Wood, J. (2018). Downscaling Changing Coastlines in a Changing Climate: The Hybrid Approach. *Journal of Geophysical Research: Earth Surface*, *123*(2), 229–251. https://doi.org/10.1002/2017JF004367

Bakker, T. M., Antolínez, J. A. A., Leijnse, T. W. B., Pearson, S. G., & Giardino, A. (2022). Estimating tropical cyclone-induced wind, waves, and surge: A general methodology based on representative tracks. *Coastal Engineering*, *176*(August 2021). https://doi.org/10.1016/j.coastaleng.2022.104154

Barnard, P. L., Erikson, L. H., Foxgrover, A. C., Hart, J. A. F., Limber, P., O'Neill, A. C., van Ormondt, M., Vitousek, S., Wood, N., Hayden, M. K., & Jones, J. M. (2019). Dynamic flood modeling essential to assess the coastal impacts of climate change. *Scientific Reports*, *9*(1), 4309. https://doi.org/10.1038/s41598-019-40742-z

Barnard, P. L., van Ormondt, M., Erikson, L. H., Eshleman, J., Hapke, C., Ruggiero, P., Adams, P. N., & Foxgrover, A. C. (2014). Development of the Coastal Storm Modeling System (CoSMoS) for predicting the impact of storms on high-energy, active-margin coasts. *Natural Hazards*, *74*(2), 1095–1125. https://doi.org/10.1007/s11069-014-1236-y

Barnard, P.L., Befus, K., Danielson, J.J., Engelstad, A.C., Erikson, L.H., Foxgrover, A., Hardy, M.W., Hoover, D.J., Leijnse, T., Massey, C., McCall, R., Nadal-Caraballo, N., Nederhoff, K., Ohenhen, L., O'Neill, A., Parker, K.A., Shirzaei, M., Su, X., Thomas, J.A., van Ormondt, M., Vitousek, S., Vos, K. and Yawn, M.C., 2023a. Future coastal hazards along the U.S. North and South Carolina coasts. *U.S. Geological Survey data release*, https://doi.org/10.5066/P9W91314

Barnard, P.L., Befus, K., Danielson, J.J., Engelstad, A.C., Erikson, L.E., Foxgrover, A., Hoover, D.J., Leijnse, T., Massey, C., McCall, R., Nadal-Caraballo, N., Nederhoff, K., Ohenhen, L., O'Neill, A., Parker, K.A., Shirzaei, M., Su, X., Thomas, J.A., van Ormondt, M., Vitousek, S.F., Vos, K., Yawn, M.C., (2023b). Future coastal hazards along the U.S. Atlantic coast. *U.S. Geological Survey data release*, https://doi.orgb/10.5066/P9BQQTCI

Bates, P. D., Quinn, N., Sampson, C., Smith, A., Wing, O. E. J., Sosa, J., Savage, J., Olcese, G., Neal, J., Schumann, G., Giustarini, L., Coxon, G., Porter, J. R., Amodeo, M. F., Chu, Z., Lewis-Gruss, S., Freeman, N. B., Houser, T., Delgado, M., … Krajewski, W. F. (2021). Combined Modeling of US Fluvial, Pluvial, and Coastal Flood Hazard Under Current and Future Climates. *Water Resources Research*, *57*(2), 1–29. https://doi.org/10.1029/2020WR028673

Bedient, P. B., Huber, W. C., & Vieux, B. E. (2013). *Hydrology and Floodplain Analysis*.

Bloemendaal, N., Haigh, I. D., de Moel, H., Muis, S., Haarsma, R. J., & Aerts, J. C. J. H. (2020). Generation of a global synthetic tropical cyclone hazard dataset using STORM. *Scientific Data*, *7*(1), 1–19. https://doi.org/10.1038/s41597-020-0381-2

Booth, J. F., Rieder, H. E., & Kushnir, Y. (2016). Comparing hurricane and extratropical storm surge for the Mid-Atlantic and Northeast Coast of the United States for 1979-2013. *Environmental Research Letters*, *11*(9). https://doi.org/10.1088/1748-9326/11/9/094004

Bruun, P. (1954). Coastal erosion and the development of beach profiles. *U.S. Army Corps of Engineers Beach Erosion Board Technical Memo*, *44*.

Callaghan, J. (2020). Extreme rainfall and flooding from Hurricane Florence. *Tropical Cyclone Research and Review*, *9*(3), 172–177. https://doi.org/10.1016/j.tcrr.2020.07.002

Chang, E. K. M., Guo, Y., & Xia, X. (2012). CMIP5 multimodel ensemble projection of storm track change under global warming. *Journal of Geophysical Research Atmospheres*, *117*(23). https://doi.org/10.1029/2012JD018578

Chemke, R., Ming, Y. & Yuval, J. (2022). The intensification of winter mid-latitude storm tracks in the Southern Hemisphere. *Nat. Clim. Chang*. https://doi.org/10.1038/s41558-022-01368-8

Church, J. A., & White, N. J. (2011). Sea-Level Rise from the Late 19th to the Early 21st Century. *Surveys in Geophysics*, *32*(4–5), 585–602. https://doi.org/10.1007/s10712-011-9119-1

CIRES. (2014). *Cooperative Institute for Research in Environmental Sciences (CIRES) at the University of Colorado, Boulder. 2014: Continuously Updated Digital Elevation Model (CUDEM). Accessed 6/30/21.* https://doi.org/10.25921/ds9v-ky35

Codiga, D. L. (2011). *Unified Tidal Analysis and Prediction Using the UTide Matlab Functions. Technical Report 2011-01. Graduate School of Oceanography, University of Rhode Island, Narragansett, RI. 59pp*. ftp://www.po.gso.uri.edu/ pub/downloads/codiga/pubs/2011Codiga-UTide-Report.pdf

CO-OPS - NOAA Tides and Currents. (2022). *Observed water levels retrieved via tidesandcurrents.noaa.gov. Accessed 15 January 2020*.

Czajkowski, J., Engel, V., Martinez, C., Mirchi, A., Watkins, D., Sukop, M. C., & Hughes, J. D. (2018). Economic impacts of urban flooding in South Florida: Potential consequences of managing groundwater to prevent salt water intrusion. *Science of The Total Environment*, *621*, 465–478. https://doi.org/10.1016/j.scitotenv.2017.10.251

Dangendorf, S., Marcos, M., Wöppelmann, G., Conrad, C. P., Frederikse, T., & Riva, R. (2017). Reassessment of 20th century global mean sea level rise. *Proceedings of the National Academy*

of Sciences of the United States of America, *114*(23), 5946–5951. https://doi.org/10.1073/pnas.1616007114

Danielson, J. J., Poppenga, S. K., Brock, J. C., Evans, G. A., Tyler, D. J., Gesch, D. B., Thatcher, C. A., & Barras, J. A. (2016). Topobathymetric elevation model development using a new methodology: Coastal national elevation database. *Journal of Coastal Research*, *76*(sp1), 75–89. https://doi.org/10.2112/SI76-008

de Bruijn, K. M. (2005). *Resilience and flood risk management; a systems approach applied to lowland rivers*. DUP Science.

Dewald, J. R., & Pike, D. A. (2014). Geographical variation in hurricane impacts among sea turtle populations. *Journal of Biogeography*, *41*(2), 307–316. https://doi.org/10.1111/jbi.12197

Doran, K. S., Long, J. W., Birchler, J. J., Brenner, O. T., Hardy, M. W., Morgan, K. L. ., Stockdon, H. F., & Torres, M. L. (2017). *Lidar-derived beach morphology (dune crest, dune toe, and shoreline) for U.S. sandy coastlines (ver. 4.0, October 2020): U.S. Geological Survey data release*. https://doi.org/10.5066/F7GF0S0Z

Dullaart, J. C. M., Muis, S., Bloemendaal, N., Chertova, M. V., Couasnon, A., & Aerts, J. C. J. H. (2021). Accounting for tropical cyclones more than doubles the global population exposed to low-probability coastal flooding. *Communications Earth & Environment*, *2*(1), 1–11. https://doi.org/10.1038/s43247-021-00204-9

Dullaart, J. C. M., Muis, S., Bloemendaal, N., & Aerts, J. C. J. H. (2020). Advancing global storm surge modelling using the new ERA5 climate reanalysis. *Climate Dynamics*, *54*(1–2), 1007–1021. https://doi.org/10.1007/s00382-019-05044-0

Eilander, D., & Boisgontier, H. (n.d.). *HydroMT*. https://doi.org/10.5281/zenodo.6961871

Erikson, L. H., Herdman, L., Flahnerty, C., Engelstad, A., Pusuluri, P., Barnard, P. L., Storlazzi, C. D., Beck, M., Reguero, B., & Parker, K. (2022). *Ocean wave time-series data simulated with a global-scale numerical wave model under the influence of projected CMIP6 wind and sea ice fields: U.S. Geological Survey data release*. https://doi.org/10.5066/P9KR0RFM

Erikson, L., Barnard, P. L., O'Neill, A., Wood, N., Jones, J., Hart, J. F., Vitousek, S., Limber, P., Hayden, M., Fitzgibbon, M., Lovering, J., & Foxgrover, A. (2018). Projected 21st century coastal flooding in the Southern California Bight. Part 2: Tools for assessing climate change-driven coastal hazards and socio-economic impacts. *Journal of Marine Science and Engineering*, *6*(3). https://doi.org/10.3390/jmse6030076

Giardino, A., Nederhoff, K., & Vousdoukas, M. (2018). Coastal hazard risk assessment for small islands : assessing the impact of climate change and disaster reduction measures on Ebeye (Marshall Islands). *Regional Environmental Change*, *2016*.

Gori, A., Lin, N., & Xi, D. (2020). Tropical Cyclone Compound Flood Hazard Assessment: From Investigating Drivers to Quantifying Extreme Water Levels. *Earth's Future*, *8*(12). https://doi.org/10.1029/2020EF001660

Guo, H., John, J. G., Blanton, C., & McHugh, C. (2018). *NOAA-GFDL GFDL-CM4 model output prepared for CMIP6 ScenarioMIP ssp585. Download 20190906. Earth System Grid Federation*. https://doi.org/10.22033/ESGF/CMIP6.9268

Han, Y., Zhang, M. Z., Xu, Z., & Guo, W. (2022). Assessing the performance of 33 CMIP6 models in simulating the large-scale environmental fields of tropical cyclones. *Climate Dynamics*, *58*(5–6), 1683–1698. https://doi.org/10.1007/s00382-021-05986-4

Hauer, M. E. (2019). Population projections for U.S. counties by age, sex, and race controlled to shared socioeconomic pathway. *Scientific Data*, *6*, 1–15. https://doi.org/10.1038/sdata.2019.5

Homer, C., Dewitz, J., Jin, S., Xian, G., Costello, C., Danielson, P., Gass, L., Funk, M., Wickham, J., Stehman, S., Auch, R., & Riitters, K. (2020). Conterminous United States land cover change patterns 2001–2016 from the 2016 National Land Cover Database. *ISPRS Journal of Photogrammetry and Remote Sensing*, *162*(February), 184–199. https://doi.org/10.1016/j.isprsjprs.2020.02.019

Huang, W., Ye, F., Zhang, Y. J., Park, K., Du, J., Moghimi, S., Myers, E., Pe'eri, S., Calzada, J. R., Yu, H. C., Nunez, K., & Liu, Z. (2021). Compounding factors for extreme flooding around Galveston Bay during Hurricane Harvey. *Ocean Modelling*, *158*, 101735. https://doi.org/10.1016/j.ocemod.2020.101735

Interagency Performance Evaluation Task Force (IPET). (2006). *Performance evaluation of the New Orleans and Southeast Louisiana Hurricane Protection System draft final report of the Interagency Performance Evaluation Task Force volume VIII – engineering and operational risk and reliability analysis.*

Jyoteeshkumar Reddy, P., Sriram, D., Gunthe, S. S., & Balaji, C. (2021). Impact of climate change on intense Bay of Bengal tropical cyclones of the post-monsoon season: a pseudo global warming approach. *Climate Dynamics*, *56*(9–10), 2855–2879. https://doi.org/10.1007/s00382-020-05618-3

Knapp, K. R., Kruk, M. C., Levinson, D. H., Diamond, H. J., & Neumann, C. J. (2010). The international best track archive for climate stewardship (IBTrACS). *Bulletin of the American Meteorological Society*, *91*(3), 363–376. https://doi.org/10.1175/2009BAMS2755.1

Knapp, K. R., Kruk, M. C., Levinson, D. H., Diamond, H. J., & Neumann, C. J. (2010). The international best track archive for climate stewardship (IBTrACS). *Bulletin of the American Meteorological Society*, *91*(3), 363–376. https://doi.org/10.1175/2009BAMS2755.1

Knutson, T. R., Sirutis, J. J., Zhao, M., Tuleya, R. E., Bender, M., Vecchi, G. A., Villarini, G., & Chavas, D. (2015). Global projections of intense tropical cyclone activity for the late twenty-first century from dynamical downscaling of CMIP5/RCP4.5 scenarios. *Journal of Climate*, *28*(18), 7203–7224. https://doi.org/10.1175/JCLI-D-15-0129.1

Kron, W. (2005). Flood Risk = Hazard • Values • Vulnerability. *Water International*, *30*(1), 58–68. https://doi.org/10.1080/02508060508691837

Le Bars, D., Drijfhout, S., & De Vries, H. (2017). A high-end sea level rise probabilistic projection including rapid Antarctic ice sheet mass loss. *Environmental Research Letters*, *12*(4). https://doi.org/10.1088/1748-9326/aa6512

Leijnse, T. W. B., Giardino, A., Nederhoff, K., & Caires, S. (2022). Generating reliable estimates of tropical-cyclone-induced coastal hazards along the Bay of Bengal for current and future climates using synthetic tracks. *Natural Hazards and Earth System Sciences*, *22*(6), 1863–1891. https://doi.org/10.5194/nhess-22-1863-2022

Leijnse, T., Nederhoff, K., Van Dongeren, A., McCall, R. T., & Van Ormondt, M. (2020). Improving computational efficiency of compound flooding simulations: The SFINCS model with subgrid features. *AGU Fall Meeting Abstracts*, *2020*, NH022--0006.

Leijnse, T., van Ormondt, M., Nederhoff, K., & van Dongeren, A. (2021). Modeling compound flooding in coastal systems using a computationally efficient reduced-physics solver: Including fluvial, pluvial, tidal, wind- and wave-driven processes. *Coastal Engineering*, *163*, 103796. https://doi.org/10.1016/j.coastaleng.2020.103796

Li, H., Sheffield, J., & Wood, E. F. (2010). Bias correction of monthly precipitation and temperature fields from Intergovernmental Panel on Climate Change AR4 models using equidistant quantile matching. *Journal of Geophysical Research Atmospheres*, *115*(10). https://doi.org/10.1029/2009JD012882

Lin, N., & Emanuel, K. (2016). Grey swan tropical cyclones. *Nature Climate Change*, *6*(1), 106–111. https://doi.org/10.1038/nclimate2777

Liu, Y. Y., Maidment, D. R., Tarboton, D. G., Zheng, X., & Wang, S. (2018). A CyberGIS Integration and Computation Framework for High-Resolution Continental-Scale Flood Inundation Mapping. *JAWRA Journal of the American Water Resources Association*, *54*(4), 770–784. https://doi.org/10.1111/1752-1688.12660

Lockwood, J. W., Oppenheimer, M., Lin, N., Kopp, R. E., Vecchi, G. A., & Gori, A. (2022). Correlation Between Sea-Level Rise and Aspects of Future Tropical Cyclone Activity in CMIP6 Models. *Earth's Future*, *10*(4), 1–19. https://doi.org/10.1029/2021EF002462

McGranahan, G., Balk, D., & Anderson, B. (2007). The rising tide: Assessing the risks of climate change and human settlements in low elevation coastal zones. *Environment and Urbanization*, *19*(1), 17–37. https://doi.org/10.1177/0956247807076960

Merkens, J. L., Reimann, L., Hinkel, J., & Vafeidis, A. T. (2016). Gridded population projections for the coastal zone under the Shared Socioeconomic Pathways. *Global and Planetary Change*, *145*, 57–66. https://doi.org/10.1016/j.gloplacha.2016.08.009

Mori, N., & Takemi, T. (2016). Impact assessment of coastal hazards due to future changes of tropical cyclones in the North Pacific Ocean. *Weather and Climate Extremes*, *11*, 53–69. https://doi.org/10.1016/j.wace.2015.09.002

Mori, N., Takemi, T., Tachikawa, Y., Tatano, H., Shimura, T., Tanaka, T., Fujimi, T., Osakada, Y., Webb, A., & Nakakita, E. (2021). Recent nationwide climate change impact assessments of natural hazards in Japan and East Asia. *Weather and Climate Extremes*, *32*, 100309. https://doi.org/10.1016/j.wace.2021.100309

Muis, S., Aerts, J. C. J. H., Dullaart, J. C., Duong, T. M., Erikson, L., Haarsma, R. J., Irazoqui, M., Mengel, M., Bars, D., Roberts, M. J., Verlaan, M., Ward, P. J., Cruz, S., & Bilt, D. (2022). *Global*

projections of storm surges using high-resolution CMIP6 climate models: validation, projected changes, and methodological challenges. 1–21. http://dx.doi.org/10.1002/essoar.10511919.1

Muis, S., Verlaan, M., Winsemius, H. C., Aerts, J. C. J. H., & Ward, P. J. (2016). A global reanalysis of storm surges and extreme sea levels. *Nature Communications*, *7*(May), 11969. https://doi.org/10.1038/ncomms11969

Murakami, H., & Sugi, M. (2010). Effect of model resolution on tropical cyclone climate projections. *Scientific Online Letters on the Atmosphere*, *6*(May), 73–76. https://doi.org/10.2151/sola.2010-019

Nadal-Caraballo, N. C., Campbell, M. O., Gonzalez, V. M., Torres, M. J., Melby, J. A., & Taflanidis, A. A. (2020). Coastal Hazards System: A Probabilistic Coastal Hazard Analysis Framework. *Journal of Coastal Research*, *95*(sp1), 1211. https://doi.org/10.2112/SI95-235.1

Nadal-caraballo, N. C., Yawn, M. C., Aucoin, L. A., Carr, M. L., Taflanidis, A. A., Kyprioti, A. P., Melby, J. A., Ramos-santiago, E., Gonzalez, V. M., Massey, T. C., Cobell, Z., & Cox, A. T. (2022). *Coastal Hazards System – Louisiana Coastal and Hydraulics. ERDC/CHL TR 22-16. Vicksburg, MS: US Army Engineer Research and Development Center. August*.

NCEI; NOAA National Centers for Environmental Information. (2022). *U.S. Billion-Dollar Weather and Climate Disasters (2022). https://www.ncei.noaa.gov/access/billions/,*. https://www.doi.org/10.25921/stkw-7w73

Nederhoff, K., Saleh, R., Tehranirad, B., Herdman, L., Erikson, L., Barnard, P. L., & van der Wegen, M. (2021). Drivers of extreme water levels in a large, urban, high-energy coastal estuary – A case study of the San Francisco Bay. *Coastal Engineering*, *170*, 103984. https://doi.org/10.1016/j.coastaleng.2021.103984

Nederhoff, K., Hoek, J., Leijnse, T., van Ormondt, M., Caires, S., & Giardino, A. (2021). Simulating synthetic tropical cyclone tracks for statistically reliable wind and pressure estimations. *Natural Hazards and Earth System Sciences*, *21*(3), 861–878. https://doi.org/10.5194/nhess-21-861-2021

NHC. (2019). Hurricane Florence. *National Hurricane Center Tropical Cyclone Report: Hurricane Florence*, *September 2018*, 1–125.

NOAA. (2022). *Climate Change: Global Sea Level on https://www.climate.gov/news-features/understanding-climate/climate-change-global-sea-level#:~:text=Global%20average%20sea%20level%20has,3.8%20inches)%20above%201993%20levels. Accessed on December 4, 2022*.

NOAA. (2021). *"National Water Model data" on https://registry.opendata.aws/nwm-archive. Accessed April 2021*.

NOAA National Geophysical Data Center. (2001). *U.S. Coastal Relief Model Vol.3 - Florida and East Gulf of Mexico. Accessed 6/30/21.* https://doi.org/10.7289/V5W66HPP

O'Neill, A., Erikson, L. H., Barnard, P. L., Limber, P. W., Vitousek, S., Warrick, J. A., Foxgrover, A. C., Lovering, J., O'Neill, A. C., Erikson, L. H., Barnard, P. L., Limber, P. W., Vitousek, S., Warrick, J. A., Foxgrover, A. C., & Lovering, J. (2018). Projected 21st century coastal flooding in the Southern

California Bight. Part 1: Development of the third generation CoSMoS model. *Journal of Marine Science and Engineering*, *6*(2), 59. https://doi.org/10.3390/jmse6020059

Parker, K., Erikson, L., Thomas, J., Nederhoff, K., Barnard, P., & Muis, S. (2022). *Relative contributions of water level components to extreme water levels along the United States Southeast Atlantic Coast from a regional-scale water level hindcast*. Submitted to 'Natural Hazards' on December 9, 2022.

Ranasinghe, R., Callaghan, D., & Stive, M. J. F. (2012). Estimating coastal recession due to sea level rise : beyond the Bruun rule. *Climatic Change*, 561–574. https://doi.org/10.1007/s10584-011-0107-8

Resio, D. T., & Irish, J. L. (2015). Tropical Cyclone Storm Surge Risk. *Current Climate Change Reports*, *1*(2), 74–84. https://doi.org/10.1007/s40641-015-0011-9

Roberts, M. (2019). *MOHC HadGEM3-GC31-HM model output prepared for CMIP6 HighResMIP highres-future. Download 20191211. Earth System Grid*. https://doi.org/10.22033/ESGF/CMIP6.5984

Roberts, M. J., Camp, J., Seddon, J., Vidale, P. L., Hodges, K., Vannière, B., Mecking, J., Haarsma, R., Bellucci, A., Scoccimarro, E., Caron, L., Chauvin, F., Terray, L., Valcke, S., Moine, M., Putrasahan, D., Roberts, C. D., Senan, R., Zarzycki, C., … Wu, L. (2020). Projected Future Changes in Tropical Cyclones Using the CMIP6 HighResMIP Multimodel Ensemble. *Geophysical Research Letters*, *47*(14). https://doi.org/10.1029/2020GL088662

Santiago-Collazo, F. L., Bilskie, M. V, & Hagen, S. C. (2019). A comprehensive review of compound inundation models in low-gradient coastal watersheds. *Environmental Modelling & Software*, *119*, 166–181. https://doi.org/10.1016/j.envsoft.2019.06.002

Scoccimarro, Enrico; Bellucci, Alessio; Peano, D. (2017). *CMCC CMCC-CM2-VHR4 model output prepared for CMIP6 HighResMIP. Version YYYYMMDD[1].Earth System Grid Federation*. https://doi.org/10.22033/ESGF/CMIP6.1367

Sebastian, A., Bader, D. J., Nederhoff, K., Leijnse, T., Bricker, J. D., & Aarninkhof, S. G. J. (2021). Hindcast of pluvial, fluvial and coastal flood damage in Houston, TX during Hurricane Harvey (2017) using SFINCS. *Natural Hazards*, *2017*. https://doi.org/10.1007/s11069-021-04922-3

Sehili, A., Lang, G., & Lippert, C. (2014). High-resolution subgrid models: background, grid generation, and implementation. *Ocean Dynamics*, *64*(4), 519–535. https://doi.org/10.1007/s10236-014-0693-x

Stockdon, H. F., Holman, R. A., Howd, P. A., & Sallenger, A. H. (2006). Empirical parameterization of setup, swash, and runup. *Coastal Engineering*, *53*(7), 573–588. https://doi.org/10.1016/j.coastaleng.2005.12.005

Sukop, M. C., Rogers, M., Guannel, G., Infanti, J. M., & Hagemann, K. (2018). High temporal resolution modeling of the impact of rain, tides, and sea level rise on water table flooding in the Arch Creek basin, Miami-Dade County Florida USA. *Science of The Total Environment*, *616–617*, 1668–1688. https://doi.org/10.1016/j.scitotenv.2017.10.170

Sweet, W. V., Hamlington, B. D., Kopp, R. E., Weaver, C. P., Barnard, P. L., Bekaert, D., Brooks, W., Craghan, M., Dusek, G., Frederikse, T., Garner, G., Genz, A. S., Krasting, J. P., Larour, E., Marcy, D., Marra, J. J., Obeysekera, J., Osler, M., Pendleton, M., … Zuzak, C. (2022). Global and Regional Sea Level Rise Scenarios for the United States. *NOAA Technical Report NOS 01*, 111 pp. https://oceanservice.noaa.gov/hazards/sealevelrise/noaa-nos-

Taherkhani, M., Vitousek, S., Barnard, P. L., Frazer, N., Anderson, T. R., & Fletcher, C. H. (2020). Sea-level rise exponentially increases coastal flood frequency. *Scientific Reports*, *10*(1), 6466. https://doi.org/10.1038/s41598-020-62188-4

Tang, W., & Carey, S. K. (2017). HydRun: A MATLAB toolbox for rainfall–runoff analysis. *Hydrological Processes*, *31*(15), 2670–2682. https://doi.org/10.1002/hyp.11185

The City of Charleston. (2015). *Sea Level Rise Strategy*. *December*, 20. https://www.charleston-sc.gov/DocumentCenter/View/10089

Thomas, J., Erikson, L., Parker, K., Barnard, P., O'Neill, A., Nadal-Caraballo, N., Massey, C., Leijnse, T., Nederhoff, K., & McCall, R. (2022). *A Comparison of Historical and Future Tropical Cyclone Activity Along the U.S. Southeast Atlantic Coast Using a CMIP6 HighResMIP Multi-Model Ensemble*. Manuscript in preperation and to be submitted to Earth's Future early 2023.

Tyler, D., Cushing, W. M., Danielson, J. J., Poppenga, S., Beverly, S. D., & Shogib, R. (2022). *Topobathymetric Model of the Coastal Carolinas, 1851 to 2020: U.S. Geological Survey data release*. https://doi.org/10.5066/P9MPA8K0

U.S. Geological Survey. (2021). *Short-Term Network Data Portal, accessed on 2021-12-23, at http://water.usgs.gov/floods/FEV/*.

U.S. Census Bureau. (2020). *2020 Population and Housing State Data for US Southeast http://censusreporter.org/Accessed 3 August 2022*.

U.S. Department of Agriculture. (1986). Urban Hydrology for Small. *Techincal Release 55*, 164. http://scholar.google.com/scholar?hl=en&btnG=Search&q=intitle:Urban+Hydrology+for+Small+watersheds#1

U.S. Department of Agriculture. (2020). *U.S. General Soil Map (STATSGO2) for Florida, Georgia, South Carolina, North Carolina and Virginia. Available online at https://gdg.sc.egov.usda.gov/ accessed on January 8, 2021*.

U.S. Enviromental Protection Agency. (2015). *Storm Water Management Model User'S Manuel. Version 5.1*. *670 /2-75–017*.

van Ormondt, M., Nederhoff, K., & Van Dongeren, A. (2020). Delft Dashboard: a quick setup tool for hydrodynamic models. *Journal of Hydroinformatics*, *22*(3), 510–527. https://doi.org/10.2166/hydro.2020.092

Vickery, P. J., Skerlj, P. F., Steckley, C., & Twisdale, L. A. (2000). Hurricane wind field model for use in hurricane simulations,. *J. Struct. Eng.*, *126*, 1203–1221.

Vitousek, S., Barnard, P., Fletcher, C. H., Frazer, N., Erikson, L., & Storlazzi, C. D. (2017). Doubling of coastal flooding frequency within decades due to sea-level rise. *Scientific Reports*, *7*(1), 1–9. https://doi.org/10.1038/s41598-017-01362-7

Volp, N. D., Van Prooijen, B. C., & Stelling, G. S. (2013). A finite volume approach for shallow water flow accounting for high-resolution bathymetry and roughness data. *Water Resources Research*, *49*(7), 4126–4135. https://doi.org/10.1002/wrcr.20324

Vousdoukas, M. I., Voukouvalas, E., Mentaschi, L., Dottori, F., Giardino, A., Bouziotas, D., Bianchi, A., Salamon, P., & Feyen, L. (2016). Developments in large-scale coastal flood hazard mapping. *Natural Hazards and Earth System Sciences*, *16*(8), 1841–1853. https://doi.org/10.5194/nhess-16-1841-2016

Wahl, T., Jain, S., Bender, J., Meyers, S. D., & Luther, M. E. (2015). Increasing risk of compound flooding from storm surge and rainfall for major US cities. *Nature Climate Change*, *5*(12), 1093–1097. https://doi.org/10.1038/nclimate2736

Y. Guo, and X. X. C. E. K. M. (2012). CMIP5 multimodel ensemble projection of storm track change under global warming. *Journal of Geophysical Research: Atmospheres*, *117*(D23), n/a-n/a. https://doi.org/10.1029/2012JD018578

Ye, F., Huang, W., Zhang, Y. J., Moghimi, S., Myers, E., Pe'eri, S., & Yu, H. C. (2021). A cross-scale study for compound flooding processes during Hurricane Florence. *Natural Hazards and Earth System Sciences*, *21*(6), 1703–1719. https://doi.org/10.5194/nhess-21-1703-2021

Appendix

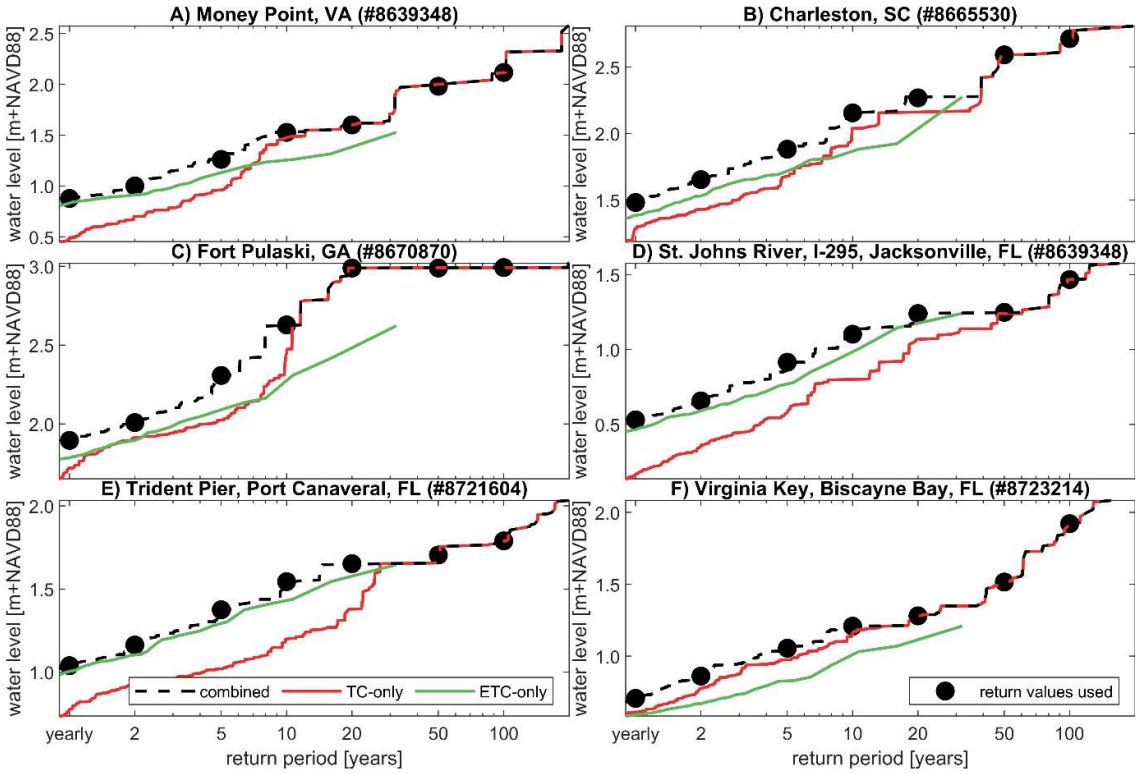

Figure 15. Extreme water level return levels and periods for TC-only simulation (red), EC-only (green) and the combined results (black dashed lines). The return values presented throughout this study are the yearly, 2-year, 5-year, 10-year, 20-year, 50-year and 100-year estimates and are shown as black dots. The dominance of ETC versus TC varies per station and return period.

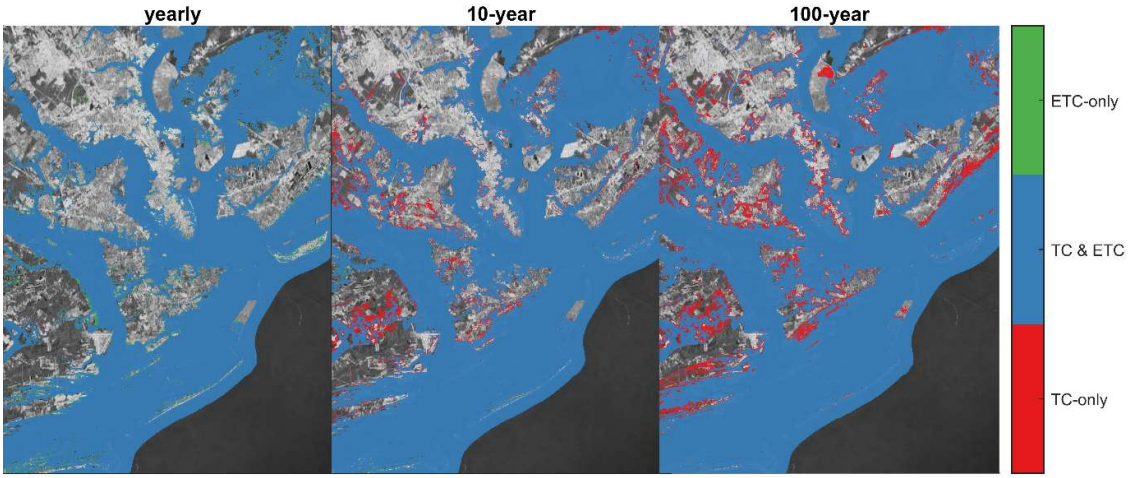

Figure 16. Breakdown of flooding for Charleston, South Carolina, for annual, 10-year and 100-year flooding. Color-coded is the source of the flooding. Most of the grid cells are flooded by both TC & ETC (either driver; blue color). Flooding with a yearly frequency is driven more by ETC-only drivers (green) while 100-year events are driven more by TC-only (red).

Table 2. Lookup table for conversion of National Land Cover Database Land to roughness values using Manning's coefficients

NLCD class	Description	Manning n
11	Open water	0.020
21	Developed, Open Space	0.070
22	Developed, Low Intensity	0.100
23	Developed, Medium Intensity	0.120
24	Developed, High Intensity	0.140
31	Barren land	0.070
41	Deciduous Forest	0.120
42	Evergreen Forest	0.150
43	Evergreen Forest	0.120
52	Evergreen Forest	0.050
71	Grassland/Herbaceous	0.034
81	Sedge/Herbaceous	0.030
82	Cultivated Crops	0.035
90	Woody Wetlands	0.100
95	Emergent Herbaceous Wetlands	0.035
	Other	0.020

Table 3. Overview of tidal skill scores for 24 NOAA and 43 XTIDE locations (68 in total)

Short name	Long name	MAE [cm]	uRMSE [cm]	bias [cm]	RMSE HW [cm]	obs_M2 [cm]	mod_M2 [cm]	obs_S2 [cm]	mod_S 2 [cm]	obs_K1 [cm]	mod_K1 [cm]
8638610	Sewells Point, VA	6.6	7.5	-0.4	3.3	35.6	34.6	6.4	5.9	5.1	4.9
8639348	Money Point, VA	19.4	22.3	-0.5	25.0	40.9	25.5	7.2	4.3	5.2	4.2
8651370	Duck, NC	12.8	14.7	-0.1	21.0	47.6	28.7	8.8	5.2	8.7	5.7
8652587	Oregon Inlet Marina, NC	26.2	30.2	0.2	29.8	12.1	2.7	2.0	0.5	2.8	0.5
8656483	Beaufort, NC	6.5	7.5	-0.6	11.5	45.1	35.4	7.2	6.2	8.0	7.1
8658120	Wilmington, NC	26.9	30.5	0.7	35.5	62.7	33.0	8.0	4.9	8.2	6.7
8658163	Wrightsville Beach, NC	4.6	5.6	-0.1	6.0	59.1	55.9	10.2	9.8	9.5	8.9
8661070	Springmaid Pier, SC	4.0	4.8	0.0	7.6	73.3	66.2	12.6	11.5	10.1	9.1
8662245	Oyster Landing, SC	9.8	11.7	-1.5	14.6	61.6	49.3	9.5	7.4	10.1	8.8
8665530	Charleston, SC	4.5	5.3	-0.9	9.3	77.0	70.5	12.1	12.8	10.4	9.6
8667633	Clarenden, SC	28.9	32.8	-5.0	26.1	108.7	97.1	16.2	18.1	11.9	10.5
8670870	Fort Pulaski, GA	8.3	9.8	0.1	14.3	101.0	87.3	16.4	16.2	11.0	10.0
8720030	Fernandina Beach, FL	4.4	5.5	-0.8	10.6	87.9	80.9	13.8	14.3	10.5	9.9
8720059	Vaughns Landing, FL	21.6	24.4	0.1	34.2	32.0	28.8	2.7	2.4	7.3	6.6
8720145	Edwards Creek, FL	16.6	19.3	-0.5	23.6	63.6	44.8	8.1	6.4	9.2	8.2
8720218	Mayport, FL	3.6	4.3	0.1	6.2	67.3	61.9	10.5	10.7	8.4	8.5
8720357	I-295 (St. Johns River), FL	5.2	6.3	0.1	8.2	13.5	6.3	1.6	1.0	2.0	1.2
8721147	Pnce de Leo, FL	9.2	10.9	-1.2	9.1	43.5	38.8	6.8	6.2	8.2	7.4
8721604	Trident Pier, FL	20.7	24.8	-1.9	25.5	50.0	37.1	7.9	6.2	9.7	7.5
8722548	PGA Bridge, Palm Beach, FL	5.0	6.1	0.6	4.4	37.5	31.7	5.9	5.0	5.8	5.6
8722588	Port of West Palm Beach, FL	1.6	1.9	-0.1	2.6	40.0	37.9	6.7	6.2	6.2	6.2
8722669	Lake Worth, FL	12.5	14.5	5.0	8.5	38.4	21.8	5.8	3.1	5.5	3.8
8723214	Virginia Key, FL	6.1	7.1	0.3	4.4	29.1	29.1	5.0	5.6	3.1	2.9
8725110	Naples, FL	4.2	5.1	0.1	4.4	26.8	29.8	8.9	10.4	14.9	13.8

8725520	Fort Myers, FL	2.2	3.1	0.1	2.6	9.6	8.4	2.9	2.6	8.2	6.8
Bear Cut	Virginia Key Bear Cut (Biscayne Bay), FL	6.2	7.2	0.3	4.2	29.8	29.2	5.2	5.6	3.1	2.9
Bings Landing	Bings Landing (Matanzas River), FL.	16.9	20.2	-0.6	19.5	20.7	14.8	2.4	2.4	4.8	4.7
Buffalo	Buffalo Bluff (St. Johns River), FL	8.1	9.5	-0.2	13.2	16.1	5.1	1.7	0.7	1.7	0.8
Canaveral	Canaveral Harbor Entrance, FL	24.2	29.2	-1.6	32.1	53.1	32.7	8.8	5.5	10.6	6.8
Capers	Capers Creek South Capers Island, SC	25.5	29.1	-2.1	35.1	69.8	47.8	11.6	7.6	10.0	8.8
Chesapeake	Chesapeake Bay Bridge, VA	3.0	3.6	-0.2	2.3	38.0	37.0	6.9	6.5	5.8	5.4
Cooper	General Dynamics Pier (Cooper River), SC	26.7	30.2	0.5	37.6	64.8	33.0	9.4	5.5	9.4	6.1
CoreSound	Sea Level Core Sound, NC	20.0	23.1	0.7	22.3	8.1	3.8	1.2	0.6	2.9	1.7
Crescent	Crescent Beach (Matanzas River), FL	25.0	28.9	-3.8	32.3	57.3	32.5	8.2	5.1	9.1	6.8
Dame Point	Dame Point (St. Johns River), FL	11.7	13.4	0.1	16.6	52.7	38.2	5.9	6.2	4.8	5.5
Daytona	Daytona Beach Shores, FL	4.5	5.4	0.1	7.3	59.5	53.5	10.6	8.8	10.0	9.1
Fernandina	Fernandina Beach (Amelia River), FL	6.4	7.7	-0.9	13.1	89.8	80.9	13.6	14.3	10.6	9.9
Hatteras	Cape Hatteras Fishing Pier, NC	19.8	23.0	-0.4	29.2	45.3	21.1	8.2	5.6	9.4	6.0
Haulover	Haulover Pier, N. Miami Beach, FL	6.2	7.5	0.0	8.6	37.3	30.0	6.9	5.6	4.3	3.5
Jacksonville	Jacksonville Long Branch, FL	9.2	10.6	0.7	12.9	37.9	26.9	5.3	4.3	4.2	3.8
Kingsbay	Kings Bay Navy Base, GA	12.2	14.3	-1.2	20.6	95.0	81.5	15.5	14.1	10.6	10.0
Kingsmill	Kingsmill (James River), VA	13.2	15.0	-0.1	14.7	33.2	24.4	5.8	3.6	5.6	3.9
LakeWorth	Lake Worth Pier, FL	3.9	4.7	0.2	6.1	41.9	36.6	7.2	6.1	5.9	5.7
Matanzas	State Road 312 (Matanzas River), FL	17.1	20.4	0.4	21.8	61.6	52.7	9.6	8.5	10.0	9.6
Mayport	Mayport ferry dock, FL	4.1	4.9	0.0	6.9	66.2	60.9	11.1	10.5	8.2	8.4
MiamiBeach	Miami Beach city pier, FL	8.3	9.8	0.1	10.6	37.3	29.3	7.5	6.0	4.2	3.2
MiamiHarbor	Government Cut Miami Harbor Entrance, FL	12.6	15.1	-0.1	15.2	34.3	28.7	6.5	5.8	3.7	3.1
NavalStation	Water Treatment Dock (St. Johns)	2.0	2.5	0.0	2.6	70.5	70.4	11.3	12.4	8.7	9.3
Ocracoke	Ocracoke Ocracoke Island, NC	25.3	29.3	0.5	29.3	13.5	2.6	2.3	0.6	3.0	0.8
Oregon	Oregon Inlet Marina Pamlico Sound, NC	8.3	9.9	-0.9	9.0	13.8	20.0	2.3	4.3	3.0	4.5
Palatka	Palatka (St. Johns River), FL	8.3	9.8	0.1	13.3	19.2	7.4	2.1	1.1	2.2	1.2
Ponce	Ponce De Leon Inlet South, FL	10.1	12.2	-1.0	10.5	44.7	38.8	6.7	6.2	8.3	7.4

Portsmouth	Portsmouth Naval Shipyard, VA	11.4	13.1	-0.7	12.4	41.3	33.8	7.3	5.7	5.9	4.8
RacyPoint	Racy Point (St. Johns River), FL	7.2	8.4	-0.1	11.1	16.6	6.5	2.4	0.9	2.3	1.2
RedBay	Red Bay Point (St Johns River), FL	5.5	6.6	-0.1	8.7	12.4	5.0	1.4	0.7	2.1	1.1
Rudee	Rudee Inlet, VA	8.2	9.6	0.2	9.9	48.5	40.0	8.9	7.2	7.5	6.3
Savannah	Savannah Bull Street, GA	32.2	36.3	-2.5	48.7	115.9	77.7	17.2	13.7	11.8	9.3
Scotland	Scotland (James River) Virginia	11.5	13.0	0.1	11.1	28.7	22.7	4.6	3.2	6.0	3.7
Southport	Southport Cape (Fear River), NC	6.5	7.5	-0.3	10.2	62.9	54.6	9.1	9.3	10.3	8.5
StAugustine	St. Augustine Beach, FL	4.3	5.0	-0.1	6.6	68.0	62.5	11.2	10.5	10.3	9.2
StHelena	St. Helena Sound	7.7	9.1	-2.3	15.9	88.3	78.6	15.2	14.5	10.6	10.0
StJohns	Main Street Bridge (St Johns River), FL	10.1	11.6	0.4	15.6	27.9	13.5	3.6	2.2	2.9	2.0
StMarys	Cut1NfrontrangeStMarysRiverFlorida	8.0	9.7	-1.0	13.4	89.3	81.6	5.8	14.5	12.3	9.9
StSimons	St. Simons Lighthouse, GA	15.0	18.2	-0.3	18.2	97.6	93.4	16.0	16.4	10.7	10.2
Sunset	Sunset Beach Pier, NC	4.7	5.8	0.0	7.2	71.7	66.1	11.5	11.5	9.7	9.1
Vilano	Vilano Beach (Tolomato River), FL	22.5	26.2	-0.2	25.0	62.3	59.6	9.4	9.9	9.6	9.6
Welaka	Welaka (St. Johns River), FL	3.9	5.6	-0.6	7.1	5.9	1.7	0.6	0.3	0.5	0.2
Wrightsville	Wrightsville Beach, NC	25.2	30.4	-1.4	29.4	59.1	43.8	10.3	7.5	9.5	7.7
	Median	8.3	9.9	-0.1	12.7	45.2	35.0	7.4	6.2	8.2	6.6